




Cite this: *New J. Chem.*, 2025, 49, 11304

# A novel core–shell $\text{Fe}_3\text{O}_4@\text{SiO}_2/\text{Co–Cr–B}$ magnetic catalyst for efficient and reusable hydrogen evolution from $\text{NaBH}_4$ hydrolysis

Housseem Lakhali,<sup>a</sup> Ömer Şahin<sup>b</sup> and Ayhan Abdullah Ceyhan  <sup>✉</sup>

This study presents a novel core–shell magnetic catalyst,  $\text{Fe}_3\text{O}_4@\text{SiO}_2/\text{Co–Cr–B}$ , engineered for efficient and reusable hydrogen generation from  $\text{NaBH}_4$  hydrolysis, offering significant advancement in sustainable hydrogen production technologies. The innovation lies in the synergistic integration of a magnetic  $\text{Fe}_3\text{O}_4@\text{SiO}_2$  core with a bimetallic Co–Cr–B shell, which enhances catalytic activity, structural stability, and facile magnetic recovery. Field emission scanning electron microscopy (FE–SEM) revealed a distinctive grape-like morphology resulting from nanoparticle agglomeration, which increased the surface area and active site accessibility. Transmission electron microscopy (TEM) confirmed a well-defined core–shell architecture with a uniform Co–Cr–B shell thickness of 40–50 nm and a consistent particle distribution. These structural features directly contribute to the catalyst's high hydrogen generation rate of  $22.2 \text{ L g}_{\text{metal}}^{-1} \text{ min}^{-1}$  at  $30^\circ\text{C}$  with a turnover frequency (TOF) of  $2110.61 \text{ mol}_{\text{H}_2} \text{ mol}_{\text{cat}}^{-1} \text{ h}^{-1}$ . The catalyst demonstrated remarkable stability and maintained >90% of its initial activity after six consecutive reusability tests. These findings highlight the potential of this catalyst for large-scale hydrogen production and offer a promising route for industrial applications with improved efficiency and durability.

Received 1st April 2025,  
Accepted 3rd June 2025

DOI: 10.1039/d5nj01445j

rsc.li/njc

## 1. Introduction

As the global demand for energy continues to rise, fossil fuels, such as oil, coal, and natural gas, still account for approximately 80% of global consumption, contributing over 400 Exajoules annually. This demand is projected to grow significantly by 23% for oil and 38% for coal.<sup>1,2</sup> However, the depletion of these limited resources and environmental concerns are two major issues associated with the heavy reliance on fossil fuels.

The combustion of fossil fuels releases hazardous pollutants, including sulfur dioxide, nitrogen dioxide, carbon monoxide, black carbon, polycyclic aromatic hydrocarbons (PAHs), and volatile chemicals, which contribute to issues such as the greenhouse effects and ground-level ozone formation ( $\text{O}_3$ ).<sup>3</sup> In response to these environmental impacts, global efforts, as highlighted in the 2015 Paris Agreement, seek to limit global temperature rise to well below  $2^\circ\text{C}$ , with an aspirational target of  $1.5^\circ\text{C}$  above pre-industrial levels.<sup>4,5</sup>

Among various renewable energy alternatives, hydrogen is particularly noteworthy because of its clean combustion

characteristics. Its oxidation produces only water as a by-product, and in the specific case of  $\text{NaBH}_4$  hydrolysis, sodium metaborate ( $\text{NaBO}_2$ ), without emitting carbon dioxide, sulfur compounds, or hydrocarbons. Moreover, hydrogen is a promising substitute for fossil fuels, as it can be sustainably produced from diverse renewable sources, such as solar, wind, and hydropower.<sup>6,7</sup> Furthermore, hydrogen has a high calorific value and high energy density ( $120\text{--}142 \text{ kJ kg}^{-1}$ ), nearly double that of gasoline, which allows more energy to be produced than conventional fuels. Its high octane number also enables operation at high compression ratios.<sup>8,9</sup> Despite these advantages, its low density is a barrier to efficient storage and transportation, necessitating advanced technological solutions. Hydrogen storage can be categorized into two main types: material-based storage and physical storage.

Material-based storage includes liquid organic hydrogen carriers (e.g., BN-methyl cyclopentane), adsorbents (e.g., MOF-5, zeolite, and carbon nanotube nanostructures), interstitial hydrides (e.g.,  $\text{LaNi}_5\text{H}_6$ ), complex hydrides (e.g.,  $\text{NaAlH}_4$ ), and chemical hydrides (e.g.,  $\text{NH}_3\text{BH}_3$ ).

Physical storage includes cryogenic liquid, pressurized gas and solid fuel as chemical/physical combination with material such as metal hydrides.<sup>10</sup>

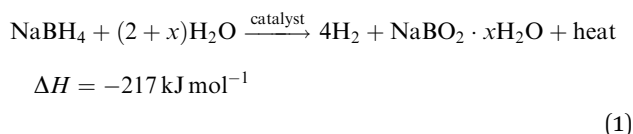
Sodium borohydride ( $\text{NaBH}_4$ ) has been identified as a promising chemical hydride for hydrogen storage and generation because of its high storage capacity (10.8 wt%), which can

<sup>a</sup> Department of Chemical Engineering, Engineering and Natural Sciences Faculty, Konya Technical University, Konya, Turkey. E-mail: lakhali@housseem91@gmail.com, aaceyhan@ktun.edu.tr

<sup>b</sup> Department of Chemical Engineering, Faculty of Chemical and Metallurgical Engineering, Istanbul Technical University, Istanbul, Turkey. E-mail: omersahin@itu.edu.tr



release hydrogen through hydrolysis at relatively low temperatures especially in the presence of a catalyst. Additionally, compared with other hydrogen carriers,  $\text{NaBH}_4$  is stable in dry air and alkaline solutions, making it safe and manageable.  $\text{NaBH}_4$  hydrolysis can be performed under ambient conditions as shown in eqn (1):



Catalysts play a crucial role in enhancing catalytic activity and hydrogen generation *via*  $\text{NaBH}_4$  hydrolysis. Various catalysts have been developed, including metal oxides,<sup>11</sup> metal-organic frameworks,<sup>12</sup> noble metals,<sup>13</sup> *etc.* However, the noble metal catalysts used for  $\text{NaBH}_4$  hydrolysis are scarce, expensive, and have limited abundance,<sup>14</sup> and the development of cost-effective non-noble metal catalysts is a priority in the industry.

Transition metal catalysts such as Co and Cr are appropriate and desirable because of their solid acids, low cost, high stability, and high catalytic activity.<sup>15</sup> For example, Callis *et al.* used a Cr-based catalyst that significantly enhanced hydrogen generation, resulting in a significant increase in catalytic activity ( $\sim 59\%$  v/v).<sup>16</sup> Co-based catalysts, particularly Co-B, are recognized for their strong performance in  $\text{NaBH}_4$  hydrolysis.<sup>14,17</sup>

However, transition-metal-based catalysts such as cobalt and chromium tend to agglomerate during the reaction, and their poor stability at high temperatures limits their use and reduces their catalytic activity.<sup>18</sup> To address these problems, core-shell structures have been explored as catalysts that can enhance catalytic performance and efficiently inhibit the migration and aggregation of nanoscale active sites owing to the protective shell.<sup>19</sup> Furthermore, core-shell architectures, particularly those employing magnetic cores like  $\text{Fe}_3\text{O}_4$ , not only increase stability by avoiding particle aggregation but also provide the special benefit of magnetic separation, thereby facilitating simple recovery, reusability, and durability of the catalyst.<sup>20</sup>

$\text{Fe}_3\text{O}_4$ , a well-known magnetic material, is particularly valued for its resistance to oxidation, acids and alkalis, low toxicity, and biocompatibility.<sup>21,22</sup> The considerable surface area of  $\text{Fe}_3\text{O}_4$  NPs allows for uniform dispersion of active catalytic sites, which enhances catalytic efficiency and boosts hydrogen generation rate.<sup>23</sup>  $\text{Fe}_3\text{O}_4$  NPs exhibit high magnetism, facilitating their efficient separation from reaction mixtures under an applied magnetic field and promoting catalyst recovery and reusability without significant performance degradation.<sup>24</sup> In the context of  $\text{NaBH}_4$  hydrolysis,  $\text{Fe}_3\text{O}_4$ -based catalysts have proven to be highly effective. For instance, F. Baye *et al.* synthesized an  $\text{Fe}_3\text{O}_4$ @C-X-Y-Co ( $\text{Fe}_3\text{O}_4$ @C core-shell) composite that achieved a hydrogen generation rate of  $1746 \text{ mL g}^{-1} \text{ min}^{-1}$  and an activation energy of  $47.3 \text{ kJ mol}^{-1}$ . This composite demonstrated excellent structural integrity and recyclability, making it promising for real-life applications with a minimal loss of catalytic activity.<sup>25</sup>

Despite these properties,  $\text{Fe}_3\text{O}_4$  tends to agglomerate during the reaction, which significantly decreases catalytic performance.

To overcome these issues, support materials including  $\text{Al}_2\text{O}_3$ ,<sup>26</sup>  $\text{TiO}_2$ ,<sup>27</sup>  $\text{CeO}_2$ ,<sup>28</sup> and carbon nanotubes<sup>29</sup> have been employed to immobilize the catalyst, prevent agglomeration, and improve catalytic performance.<sup>30</sup>

$\text{SiO}_2$ , in particular, is an excellent support material for  $\text{Fe}_3\text{O}_4$  NPs, preventing agglomeration by reducing magnetic dipole interactions and maintaining a uniform distribution of nanoparticles. In addition,  $\text{SiO}_2$  provides a high surface-to-volume ratio, which enhances its ability to interact with other substances and improves the performance of chemical reactions.<sup>21</sup> In recent studies,  $\text{Fe}_3\text{O}_4$ @ $\text{SiO}_2$  core-shell structures have demonstrated excellent performance in hydrogen generation, attributed to their high surface area and effective dispersion of active sites. For instance, Dou *et al.* synthesized a  $\text{Ru/CoO}_x$ @NPC catalyst using a core-shell metal-organic framework (MOF) as a template, achieving a hydrogen generation rate of  $8.01 \text{ L min}^{-1} \text{ g}^{-1}$  with a turnover frequency, TOF, of  $1118.6 \text{ mol}_{\text{H}_2} \text{ min}^{-1} \text{ mol}_{\text{Ru}}^{-1}$ .<sup>31</sup>

This work focuses on the synthesis and characterization of a new  $\text{Fe}_3\text{O}_4$ @ $\text{SiO}_2$ /Co-Cr-B core-shell magnetically separable catalyst for hydrogen generation from  $\text{NaBH}_4$  hydrolysis, contributing to the broader context of the green energy transition. While previous studies have explored  $\text{Fe}_3\text{O}_4$ -based catalysts and core-shell structures for this reaction, this work distinguishes itself by the specific combination of a  $\text{Fe}_3\text{O}_4$ @ $\text{SiO}_2$  core-shell structure and a Co-Cr-B active catalytic layer. This unique combination is hypothesized to offer several advantages crucial for practical application in a sustainable hydrogen economy: (i) the  $\text{Fe}_3\text{O}_4$  core provides magnetic separability for easy catalyst recovery and reuse, minimizing waste and resource consumption, directly supporting circular economy principles; (ii) the  $\text{SiO}_2$  shell acts as a support to prevent  $\text{Fe}_3\text{O}_4$  agglomeration and enhance the dispersion of the active catalytic sites, maximizing their availability for the reaction and improving long-term catalyst performance, a key factor for cost-effective hydrogen production; and (iii) the Co-Cr-B ternary metal boride catalytic layer, instead of a single metal or binary metal boride, is expected to exhibit synergistic effects, potentially leading to enhanced catalytic activity and stability compared to Co-B or Cr-B catalysts alone. This combination is relatively unexplored in the context of  $\text{NaBH}_4$  hydrolysis, and offers a promising avenue for developing highly active, stable, and cost-effective catalysts. Cost effectiveness and durability are essential for the widespread adoption of hydrogen as a clean energy carrier.

Furthermore, this study systematically investigates the influence of key reaction parameters, including the catalyst amount, NaOH and  $\text{NaBH}_4$  concentrations, and reaction temperature, on the hydrogen generation rate. The reusability of the catalyst is also evaluated, which is crucial for real-world applications and reducing the environmental footprint of catalyst synthesis. A comprehensive characterization of the synthesized catalyst is performed using XRD, FE-SEM, EDX, BET, TEM, XPS, and FTIR techniques to establish structure-property relationships and provide insights into the catalytic mechanism. This detailed investigation aims to demonstrate the superior performance of the novel  $\text{Fe}_3\text{O}_4$ @ $\text{SiO}_2$ /Co-Cr-B catalyst for efficient and sustainable hydrogen generation, a critical component of the



transition away from fossil fuels and towards a cleaner hydrogen-based energy future.

## 2. Materials and methods

### 2.1. Materials

Ferric(III) chloride hexahydrate ( $\text{FeCl}_3 \cdot 6\text{H}_2\text{O}$ ), sodium borohydride ( $\text{NaBH}_4$ ), cobalt(II) chloride hexahydrate ( $\text{CoCl}_2 \cdot 6\text{H}_2\text{O}$ ), chromium(III) nitrate nonahydrate ( $\text{Cr}(\text{NO}_3)_3 \cdot 9\text{H}_2\text{O}$ ), ethanol ( $\geq 95\%$ ), sodium acetate, trisodium citrate, ethylene glycol, tetraethyl orthosilicate (TEOS, 98%) and concentrated ammonia solution (28 wt%) were all acquired from Merck company. De-ionized water was obtained from ILTEK (Selçuk University).

### 2.2. Methods

**2.2.1. Synthesis of  $\text{Fe}_3\text{O}_4$ .**  $\text{Fe}_3\text{O}_4$  nanoparticles were synthesized using a hydrothermal method, while  $\text{Fe}_3\text{O}_4@/\text{SiO}_2$  core-shell structures were produced through the Stöber process. Under magnetic stirring, 1.08 g of  $\text{FeCl}_3 \cdot 6\text{H}_2\text{O}$  was dissolved in 20 mL of ethylene glycol. This solution was then treated with 1.8 g of sodium acetate and agitated for an hour. Subsequently, the solution was mixed with 0.25 g of trisodium citrate and agitated for 30 min to ensure homogeneous dispersion. The resulting mixture was then transferred to a Teflon-lined stainless steel autoclave and heated at 200 °C for 10 h. After cooling, the black magnetic particles were collected with a magnet, washed 3–4 times with deionized water and ethanol, and then vacuum-dried for 12 h at 50 °C.

**2.2.2. Synthesis of  $\text{Fe}_3\text{O}_4@/\text{SiO}_2$ .** To coat the  $\text{Fe}_3\text{O}_4$  nanoparticles with a silica shell, 0.1 g of  $\text{Fe}_3\text{O}_4$  NPs was dispersed by sonication for 1 h in a solution containing 40 mL of ethanol, 10 mL of deionized water, and 1.2 mL of concentrated aqueous ammonia. After achieving a uniform dispersion, 0.35 mL of tetraethyl orthosilicate (TEOS) was added dropwise to the solution. After stirring for 2 h, the resulting  $\text{Fe}_3\text{O}_4@/\text{SiO}_2$  products were collected, washed with deionized water, and vacuum-dried for 12 h at 60 °C.<sup>32</sup>

**2.2.3. Synthesis of  $\text{Fe}_3\text{O}_4@/\text{SiO}_2/\text{Co-Cr-B}$ .** To synthesize the  $\text{Fe}_3\text{O}_4@/\text{SiO}_2/\text{Co-Cr-B}$  catalyst, an aqueous solution containing cobalt(II) chloride hexahydrate ( $\text{CoCl}_2 \cdot 6\text{H}_2\text{O}$ ) and chromium(III) nitrate nonahydrate ( $\text{Cr}(\text{NO}_3)_3 \cdot 9\text{H}_2\text{O}$ ) was vigorously stirred with  $\text{Fe}_3\text{O}_4@/\text{SiO}_2$ . Sodium borohydride ( $\text{NaBH}_4$ ) was then added as a

reducing agent, leading to the formation of Co–Cr–B nanoparticles on  $\text{Fe}_3\text{O}_4@/\text{SiO}_2$  core-shell structures. The resulting black powder residue was filtered, thoroughly washed with deionized water, hot deionized water, and ethanol and subsequently dried under  $\text{N}_2$  gas at 80 °C for 5 h (Fig. 1).

### 2.3. Catalytic hydrogen generation from $\text{NaBH}_4$ hydrolysis

The initial  $\text{NaBH}_4$  hydrolysis process was studied using a solution containing 1%  $\text{NaBH}_4$ , 3%  $\text{NaOH}$ , and 100 mg of catalyst. The process temperature was set to 30 °C with a total solution volume of 10 mL. Several key parameters were systematically varied to optimize the  $\text{NaBH}_4$  hydrolysis process, including the  $\text{NaOH}$  concentration (3, 5, 7, and 10%),  $\text{NaBH}_4$  concentration (1, 3, 5, and 7%), catalyst amount (25, 50, 75, and 100 mg), and temperature (20, 30, 40, and 50 °C).

The catalyst was initially placed in a reaction flask connected to a gas collection system consisting of an exit tube leading to an inverted water-filled gas burette for volume measurement. Prepared solutions of  $\text{NaBH}_4$  and  $\text{NaOH}$  were added to the catalyst in the flask without agitation to maintain consistency in the reaction kinetics. The hydrogen gas produced was directed through the tubing, displacing the water in the burette. The volume of displaced water was recorded as a direct measure of hydrogen gas generation.

It was assumed that  $\text{H}_2$  was the sole gaseous product of  $\text{NaBH}_4$  hydrolysis under the studied conditions, as commonly reported in the literature. However, in the absence of direct gas-phase analysis (*e.g.*, GC or MS), this assumption is acknowledged as a limitation of the present study.

### 2.4. Characterization

The synthesized catalyst was characterized using X-ray diffraction (XRD), field emission scanning electron microscopy (FE-SEM), energy dispersive X-ray spectroscopy (EDX), Brunauer–Emmett–Teller (BET), X-ray photoelectron spectroscopy (XPS), transmission electron microscopy (TEM) and Fourier transform infrared spectroscopy (FTIR). An FTIR spectrometer (Thermo Scientific Nicolet 380) was used to identify the functional groups in the structure ( $4000\text{--}400\text{ cm}^{-1}$ ). FE-SEM and EDX (Zeiss Sigma 300) instruments were used for the structural study of the catalyst and elemental analysis, respectively. The crystal structure and phase purity of the synthesized catalysts were determined by XRD



Fig. 1 Schematic representation of catalyst preparation.



(Bruker D8 Advance) using CuK ( $\lambda = 1.54060$ ) radiation. A BET instrument (Quantachrome Nova 1200) was used to investigate the surface area of the catalyst. A PHI 5000 Versa Probe spectrometer was used to conduct X-ray photoelectron spectroscopy (XPS) in order to investigate the surface electronic states of the produced catalyst. The JEOL JEM-1010 transmission electron microscope (TEM) is well-known for its ability to analyze materials at the elemental level, take high-resolution images, and investigate materials at the atomic level.

### 3. Results and discussion

#### 3.1. Fourier transform infrared spectroscopy (FTIR) analysis

Fourier transform infrared spectroscopy (FTIR) was utilized to identify the functional groups in the synthesized catalyst, specifically examining the  $\text{Fe}_3\text{O}_4$ ,  $\text{Fe}_3\text{O}_4@\text{SiO}_2$ , and  $\text{Fe}_3\text{O}_4@\text{SiO}_2@\text{Co-Cr-B}$  composite materials.

The FTIR spectrum of  $\text{Fe}_3\text{O}_4$  (Fig. 2-a) exhibited a prominent absorption peak at approximately  $590\text{ cm}^{-1}$ , which corresponds

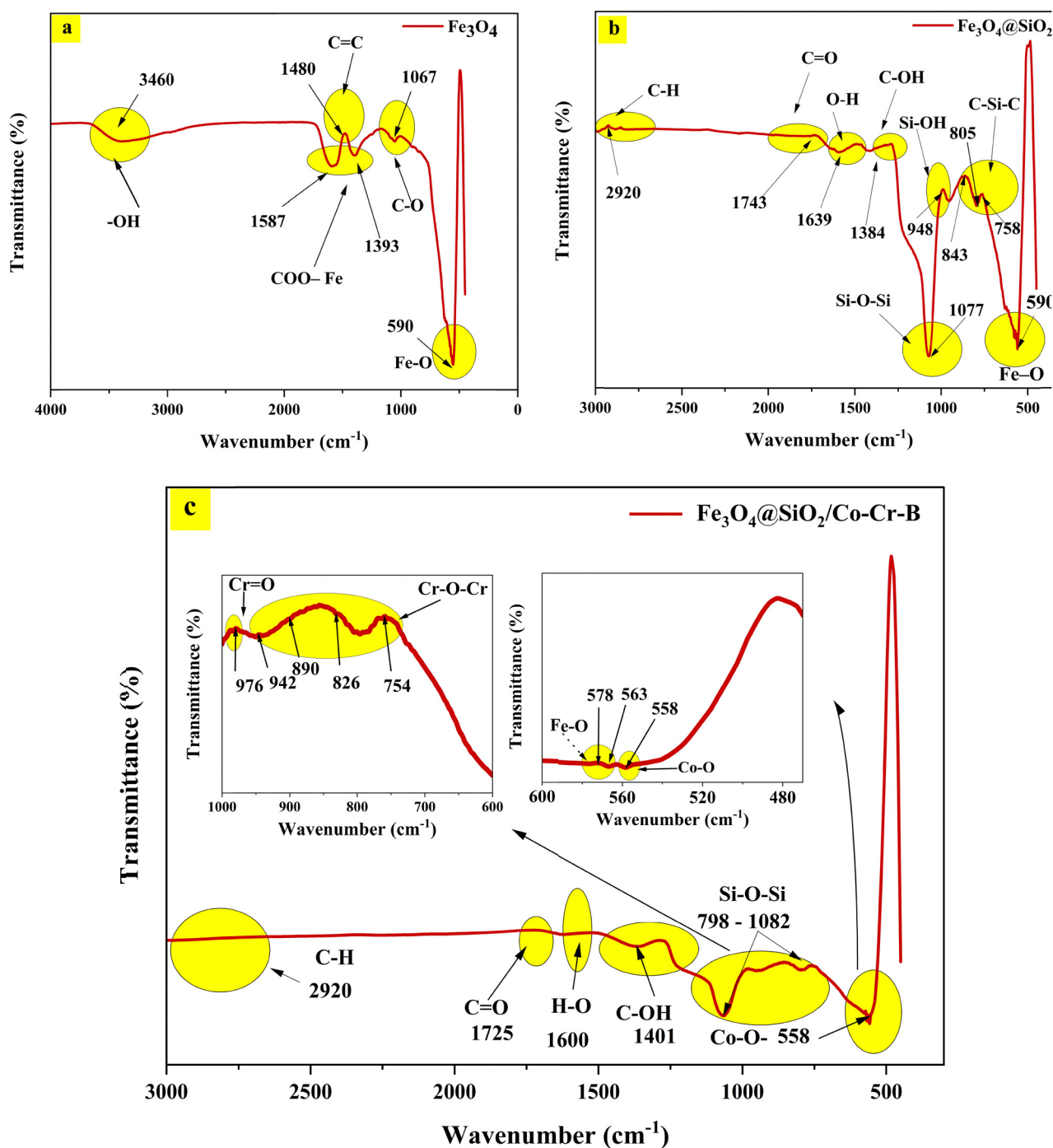
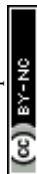


Fig. 2 FTIR spectrum of (a)  $\text{Fe}_3\text{O}_4$ , (b)  $\text{Fe}_3\text{O}_4@\text{SiO}_2$  and (c)  $\text{Fe}_3\text{O}_4@\text{SiO}_2/\text{Co-Cr-B}$ .





to the stretching vibration mode of Fe–O bonds in Fe<sub>3</sub>O<sub>4</sub>, occupying tetrahedral positions.<sup>33</sup> The C–O stretching vibration of epoxide was observed at 1067 cm<sup>−1</sup>.<sup>34</sup> The characteristic peaks observed at wavenumbers of 1393 cm<sup>−1</sup> and 1587 cm<sup>−1</sup> corresponding to the COO–Fe bond were likely formed due to the interaction between the carboxylate anion of sodium citrate and the hydroxide radical present on the Fe<sub>3</sub>O<sub>4</sub> surface.<sup>35</sup> A typical hydroxyl group (–OH) bond peak was observed at approximately 3378–3400 cm<sup>−1</sup>, indicating the successful binding of sodium citrate to the Fe<sub>3</sub>O<sub>4</sub> surface.<sup>36</sup>

The FTIR spectrum of Fe<sub>3</sub>O<sub>4</sub>@SiO<sub>2</sub> (Fig. 2-b) also exhibited a peak around 580 cm<sup>−1</sup>, which is again associated with the Fe–O bond vibrations of Fe<sub>3</sub>O<sub>4</sub> at the Fe–O<sub>6</sub> (octahedral) sites.<sup>37</sup> Peaks observed at 758 cm<sup>−1</sup> and 843 cm<sup>−1</sup> indicate the presence of C–Si–C stretching vibrations,<sup>38</sup> while an additional peak at 948 cm<sup>−1</sup> corresponds to Si–OH stretching and bending vibrations.<sup>39</sup> The prominent peaks at 805 cm<sup>−1</sup> and 1077 cm<sup>−1</sup> were attributed to the asymmetric (*v*<sub>as</sub>) and symmetric (*v*<sub>s</sub>) stretching vibrations of the Si–O–Si bonds, respectively.<sup>40</sup> The C=O and C–OH stretching vibrations of the carboxyl groups (–COOH) contributed to the peaks at 1743 cm<sup>−1</sup> and 1384 cm<sup>−1</sup> respectively, while the peak at 1639 cm<sup>−1</sup> was due to the bending vibration of the hydroxyl (–OH) group.<sup>41,42</sup> Finally, in this spectrum, the peak at 2920 cm<sup>−1</sup> was attributed to the C–H stretching vibration.<sup>43</sup>

The FTIR spectrum of Fe<sub>3</sub>O<sub>4</sub>@SiO<sub>2</sub>/Co–Cr–B (Fig. 2-c) displayed peaks in the range of 563 cm<sup>−1</sup> to 578 cm<sup>−1</sup> corresponding to the Fe–O bond vibrations.<sup>44,45</sup> However, the peaks at 798 cm<sup>−1</sup> and 1082 cm<sup>−1</sup> are attributed to the presence of Si–O–Si bonds.<sup>46,47</sup> The peak at 976 cm<sup>−1</sup> was assigned to the Cr=O bending vibration, indicating the presence of Cr in its oxidation state. The peaks at 826 cm<sup>−1</sup>, 890 cm<sup>−1</sup>, and 942 cm<sup>−1</sup> were associated with Cr(vi), resulting from Cr–O–Cr bond vibrations.<sup>48,49</sup> The peak at 558 cm<sup>−1</sup> is attributed to the Co–O vibration.<sup>50,51</sup> The bending vibration of the hydroxyl (–OH) group was responsible for the peak at 1639 cm<sup>−1</sup>, while the carboxyl group (–COOH) C=O and C–OH stretching vibrations contributed to the peaks at 1743 cm<sup>−1</sup> and 1384 cm<sup>−1</sup>, respectively.<sup>41,42</sup>

### 3.2. Field emission scanning electron microscopy (FE-SEM-EDX)

Field emission scanning electron microscopy (FE-SEM) was used to study the structure of the catalyst and provide detailed insights into its morphology, while energy dispersive X-ray spectroscopy (EDX) was used to determine the elemental composition and distribution within the catalyst.

The surface morphologies of the synthesized catalysts were examined using field-emission scanning electron microscopy (FE-SEM) on a Zeiss Sigma 300 instrument. Prior to imaging, the samples were gently ground and uniformly dispersed onto conductive carbon tape mounted on an aluminum SEM stub. To prevent charging during the analysis, the samples were coated with a thin conductive layer of gold using a sputter coater. Imaging was carried out under high-vacuum conditions using an accelerating voltage of 5–10 kV and optimized to obtain high-resolution micrographs without damaging the sample structure.

For elemental composition analysis, energy-dispersive X-ray spectroscopy (EDX) was conducted using the same Zeiss Sigma 300 system equipped with an Oxford Instruments EDX detector. EDX spectra were collected at an accelerating voltage of 15–20 kV to ensure sufficient X-ray generation and signal clarity. Elemental mapping and quantification were performed to confirm the presence and distribution of the key elements (Fe, Al, Co, Cs, O, C, *etc.*) in the catalyst structure.

As shown in the FE-SEM image in Fig. 3-a, the magnetic effect causes the particles to agglomerate, which is a common characteristic of Fe<sub>3</sub>O<sub>4</sub>.<sup>52</sup> Based on the obtained particles, the catalyst predominantly consists of particles in the 100–200 nm range. The Fe<sub>3</sub>O<sub>4</sub> NPs appear highly spherical and exhibit a rough surface texture with a proportional distribution.<sup>53</sup>

The energy dispersive X-ray (EDX) results (Fig. 3-b) confirmed the efficient synthesis of Fe<sub>3</sub>O<sub>4</sub>, composed of 66.7 wt% Fe and 33.3 wt% O.

From the FE-SEM image of Fig. 3-c, it was observed that coating Fe<sub>3</sub>O<sub>4</sub> with SiO<sub>2</sub> decreased agglomeration, and the surface of the catalyst became smooth, with a particle size of approximately 200 nm. The SiO<sub>2</sub>-coated Fe<sub>3</sub>O<sub>4</sub> nanoparticles maintained a spherical shape and were well-distributed, which suggests improved dispersion and stability.

In contrast, the EDX spectrum of Fe<sub>3</sub>O<sub>4</sub>@SiO<sub>2</sub> (Fig. 3-d) shows that the percentages of Fe, O, C, and Si were 24.3 wt%, 30.3 wt%, 38.4 wt% and 7.1 wt%, respectively.

The adsorption of Co and Cr on the Fe<sub>3</sub>O<sub>4</sub>@SiO<sub>2</sub> surface produced a catalytic surface (Fig. 3-e) characterized by a consistent size distribution and structure, with particle agglomeration forming a grape-like morphology. This morphology increased the active surface area of the catalysts, enhancing their interaction with NaBH<sub>4</sub> for hydrogen generation.<sup>52</sup>

For Fe<sub>3</sub>O<sub>4</sub>@SiO<sub>2</sub>/Co–Cr–B (Fig. 2-f), the percentages of Co, Si, Fe, Cr, and C were 35.6 wt%, 7.7 wt%, 15.01 wt%, 0.6 wt%, and 13.0 wt%, respectively. Additionally, carbon (13.0 wt%) was detected, which is most likely attributed to the carbon coating applied to the FE-SEM sample holder.<sup>54</sup>

However, the “O” contents of Fe<sub>3</sub>O<sub>4</sub>, Fe<sub>3</sub>O<sub>4</sub>@SiO<sub>2</sub>, and Fe<sub>3</sub>O<sub>4</sub>@SiO<sub>2</sub>/Co–Cr–B are 33.3 wt%, 40.1 wt%, and 28.1 wt%, respectively. When Fe<sub>3</sub>O<sub>4</sub> nanoparticles were coated with SiO<sub>2</sub>, the total oxygen concentration increased from 33.3 wt% (Fe<sub>3</sub>O<sub>4</sub>) to 40.1 wt% (Fe<sub>3</sub>O<sub>4</sub>@SiO<sub>2</sub>). The FTIR results suggest that the silica surface may contain hydroxyl groups (Si–OH) produced by water interactions, contributing to the overall oxygen concentration.<sup>38</sup> In the Fe<sub>3</sub>O<sub>4</sub>@SiO<sub>2</sub>/Co–Cr–B catalyst, the high oxygen content is associated with characteristic bond vibrations corresponding to Cr–O–Cr and Co–O bonds, indicating an increased incorporation of oxygen within the material.<sup>48,51</sup>

The EDX map of Fe<sub>3</sub>O<sub>4</sub> (Fig. 3-g) reveals the elemental composition confirming the presence of Fe and O, with a uniform distribution of Fe and O throughout the Fe<sub>3</sub>O<sub>4</sub> surface supporting the high purity and uniformity of the synthesized Fe<sub>3</sub>O<sub>4</sub> NPs.

The EDX map of Fe<sub>3</sub>O<sub>4</sub>@SiO<sub>2</sub> in Fig. 3-h shows the presence of Fe, O, and Si, confirming the successful coating of Fe<sub>3</sub>O<sub>4</sub> NPs with SiO<sub>2</sub>. The Fe signals were primarily concentrated in the core region, while Si and O were found surrounding Fe.



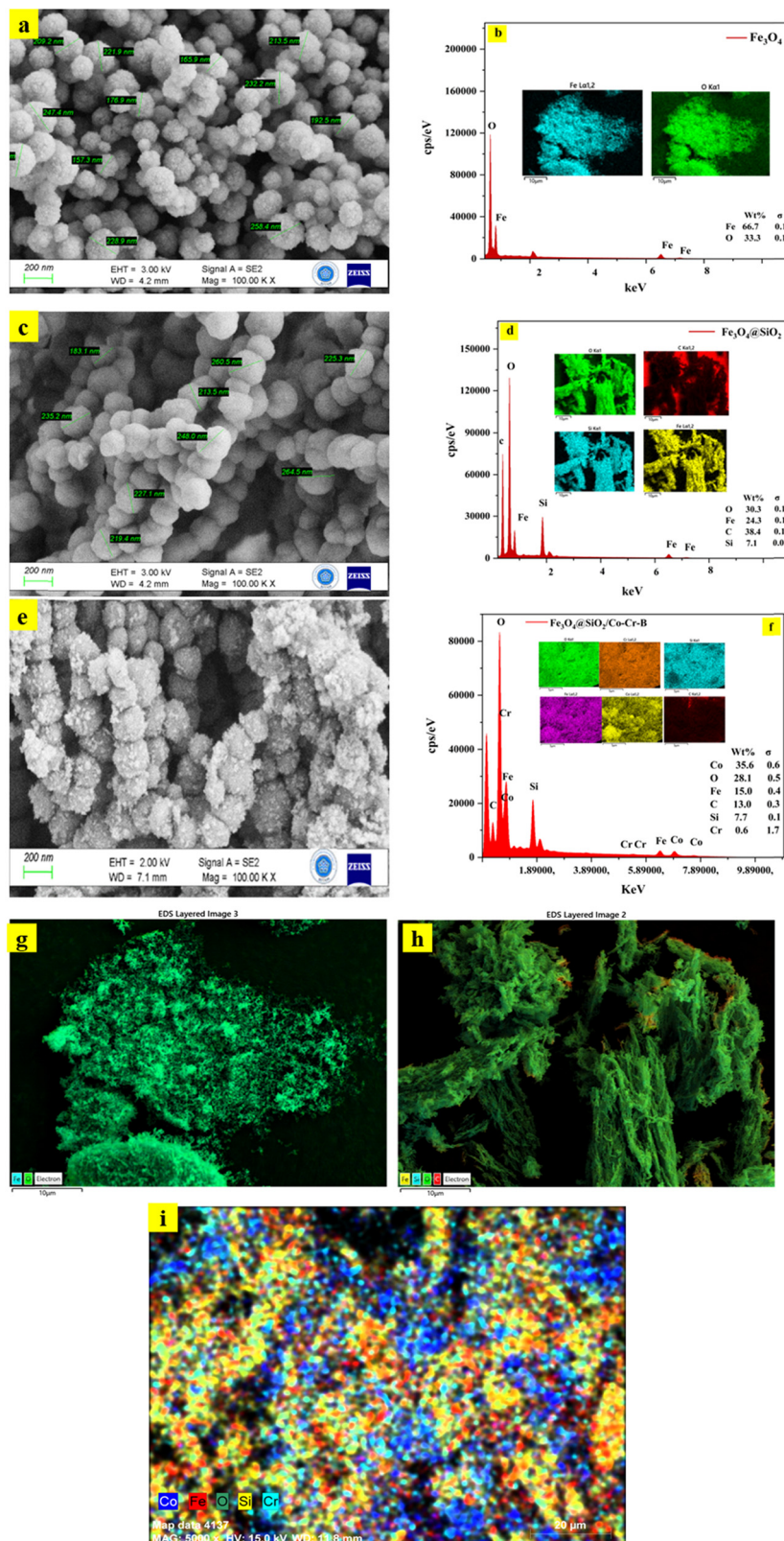
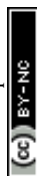


Fig. 3 FESEM images/EDX spectrum/EDX map image of (a), (b) and (g)  $\text{Fe}_3\text{O}_4$ , (c), (d) and (h)  $\text{Fe}_3\text{O}_4@ \text{SiO}_2$  and (e), (f) and (i)  $\text{Fe}_3\text{O}_4@ \text{SiO}_2/\text{Co-Cr-B}$ .

The EDX map image of  $\text{Fe}_3\text{O}_4@ \text{SiO}_2/\text{Co-Cr-B}$  in Fig. 2-i reveals a uniform and homogeneous distribution of the elements throughout the catalyst surface, with distinct signals for Fe, O, Si, Co, and

Cr. This composite system is expected to exhibit enhanced magnetic and catalytic properties owing to the synergistic interaction between the  $\text{Fe}_3\text{O}_4$  core, the  $\text{SiO}_2$  shell and the Co-Cr-B layer.



### 3.3. Transmission electron microscopy analysis

Transmission electron microscopy (TEM) was used to obtain high-resolution images of the interior structure of the produced samples at the atomic or nanometer scale.

The TEM image (Fig. 4-a and b) of the synthesized  $\text{Fe}_3\text{O}_4@\text{SiO}_2/\text{Co-Cr-B}$  clearly demonstrates the core-shell structure. The core is composed of the dark  $\text{Fe}_3\text{O}_4$  which is known for its magnetic properties. This core is essential for applications requiring magnetic separation.<sup>55</sup> The  $\text{Fe}_3\text{O}_4$  cores are surrounded by a uniform gray  $\text{SiO}_2$  layer, which acts as a protective and stabilizing intermediate shell,<sup>56,57</sup> followed by an outer Co-Cr-B layer with a reported thickness of approximately 40–50 nm which is clearly distinguishable in the TEM images.

The overall particle shape was mostly spherical, which is advantageous for achieving uniform coating and enhancing the surface area. This spherical morphology also facilitates better dispersion of the catalyst in reactive systems, promoting effective interactions with reactants such as  $\text{NaBH}_4$  for hydrogen generation. The observed core-shell structure and particle morphology are in line with expected outcomes of the synthesis strategy in the literature and further confirm the successful integration of  $\text{Fe}_3\text{O}_4$ ,  $\text{SiO}_2$ , and Co-Cr-B into a single composite system.<sup>58</sup>

### 3.4. X-ray diffraction (XRD) analysis

XRD analysis was conducted to determine the crystal structure and phase purity of the synthesized nanoparticles, specifically investigating the phases of the as-prepared  $\text{Fe}_3\text{O}_4$ ,  $\text{Fe}_3\text{O}_4@\text{SiO}_2$ , and  $\text{Fe}_3\text{O}_4@\text{SiO}_2/\text{Co-Cr-B}$  composites. In the XRD pattern shown in Fig. 5-a, the characteristic diffraction peaks observed at  $2\theta$  peaks of  $30.1^\circ$ ,  $35.4^\circ$ ,  $43.2^\circ$ ,  $53.6^\circ$ ,  $57.1^\circ$ , and  $63.0^\circ$  are attributed to the  $\text{Fe}_3\text{O}_4$  NPs. These peaks correspond to the (220), (311), (400), (422), (511), and (440) crystal planes, respectively, which can be indexed to the face-centered cubic structure of magnetite (JCPDS card no. 19-0629).<sup>37,59</sup> However, the absence of any other peaks indicated that the synthesized  $\text{Fe}_3\text{O}_4$  nanoparticles had a high degree of purity.

Fig. 5-b displays the XRD pattern for  $\text{Fe}_3\text{O}_4@\text{SiO}_2$ , which shows slight deviations from the  $\text{Fe}_3\text{O}_4$  pattern with peaks at  $2\theta = 31.39^\circ$ ,  $36.63^\circ$ ,  $44.08^\circ$ ,  $54.66^\circ$ ,  $58.24^\circ$ , and  $63.88^\circ$ . These shifts provide evidence for the presence of  $\text{SiO}_2$  in an amorphous state and show that its introduction does not change the crystalline structure of  $\text{Fe}_3\text{O}_4$ .<sup>60</sup>

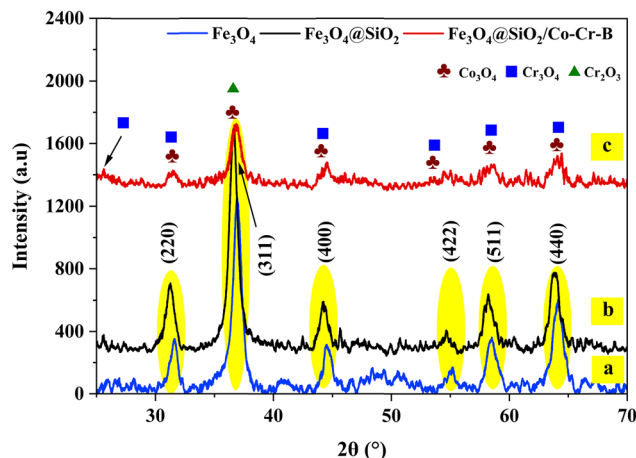


Fig. 5 XRD pattern of (a)  $\text{Fe}_3\text{O}_4$ , (b)  $\text{Fe}_3\text{O}_4@\text{SiO}_2$  and (c)  $\text{Fe}_3\text{O}_4@\text{SiO}_2/\text{Co-Cr-B}$ .

In Fig. 5-c, the XRD pattern of the synthesized catalyst demonstrates diffraction peaks of cobalt and chromium oxides overlapping with those of  $\text{Fe}_3\text{O}_4$ , indicating the presence of this magnetic core, which is essential for the magnetic properties and ease of recovery of the catalyst.<sup>61</sup> Peaks at approximately  $2\theta = 31.2^\circ$ ,  $36.6^\circ$ ,  $44.7^\circ$ ,  $54.66^\circ$ ,  $59.1^\circ$ , and  $65.2^\circ$  corresponding to the (220), (311), (400), (511) and (440) planes suggest the formation of  $\text{Co}_3\text{O}_4$  (JCPDS Card No. 96-900-5888).<sup>62</sup> In addition, the presence of  $\text{Cr}_2\text{O}_3$  is indicated by a peak at approximately  $2\theta = 35^\circ$ .<sup>63</sup> The peaks at approximately  $2\theta = 23.0^\circ$ ,  $32.7^\circ$ ,  $45^\circ$ ,  $53^\circ$ ,  $58.2^\circ$ , and  $68.5^\circ$  correspond to  $\text{Cr}_3\text{O}_4$ , according to the JCPDS File No. 12-559.<sup>64</sup> The hydrolysis of  $\text{NaBH}_4$  was greatly improved by the combination of  $\text{Fe}_3\text{O}_4$ ,  $\text{Co}_3\text{O}_4$ , and  $\text{Cr}_2\text{O}_3$ . Co and Cr oxides boost catalytic activity by increasing the surface area and electrical interactions, while the  $\text{Fe}_3\text{O}_4$  core offers magnetic characteristics for simple separation and reuse.<sup>61,65,66</sup>

### 3.5. Brunauer-Emmett-Teller (BET) analysis

The specific surface area of the synthesized catalyst was calculated using Brunauer-Emmett-Teller (BET) analysis. The specific surface areas of  $\text{Fe}_3\text{O}_4$ ,  $\text{Fe}_3\text{O}_4@\text{SiO}_2$ , and  $\text{Fe}_3\text{O}_4@\text{SiO}_2/\text{Co-Cr-B}$  are presented in Table 1.

According to the BET data, the specific surface areas of the synthesized  $\text{Fe}_3\text{O}_4$ ,  $\text{Fe}_3\text{O}_4@\text{SiO}_2$ , and  $\text{Fe}_3\text{O}_4@\text{SiO}_2/\text{Co-Cr-B}$

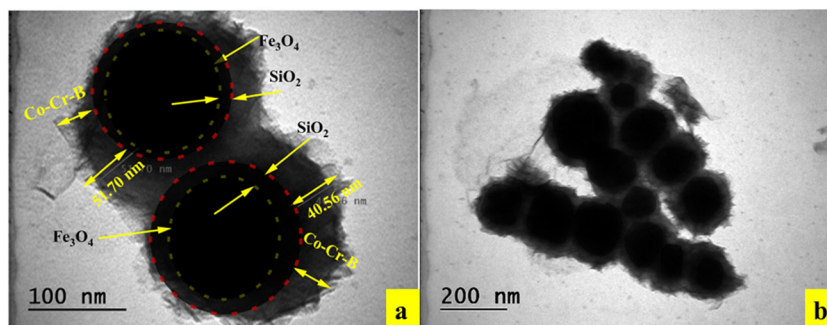


Fig. 4 TEM image of  $\text{Fe}_3\text{O}_4@\text{SiO}_2/\text{Co-Cr-B}$ .





**Table 1** The BET results of  $\text{Fe}_3\text{O}_4$ ,  $\text{Fe}_3\text{O}_4@\text{SiO}_2$ , and  $\text{Fe}_3\text{O}_4@\text{SiO}_2/\text{Co-Cr-B}$ 

Textural properties	$\text{Fe}_3\text{O}_4$	$\text{Fe}_3\text{O}_4@\text{SiO}_2$	$\text{Fe}_3\text{O}_4@\text{SiO}_2/\text{Co-Cr-B}$
Surface area ( $\text{m}^2 \text{g}^{-1}$ )	53.39	27.08	46.67
Pore diameter (nm)	13.24	13.85	9.47

catalysts were 53.39, 27.08, and  $46.67 \text{ m}^2 \text{g}^{-1}$ , respectively. However, the results indicated a decrease in the surface area of  $\text{Fe}_3\text{O}_4@\text{SiO}_2$  compared to that of  $\text{Fe}_3\text{O}_4$ . This decrease is attributed to  $\text{SiO}_2$  coating, which leads to blockage of the surface pores through adsorption. Similar observations have been reported previously.<sup>21,67</sup>

Interestingly, upon the adsorption of metals onto the  $\text{Fe}_3\text{O}_4@\text{SiO}_2$  surface, the surface area increased significantly to  $46.67 \text{ m}^2 \text{g}^{-1}$ . For instance, Vishwanath *et al.* synthesized  $\text{TiO}_2$  as a support, while Madona *et al.* synthesized  $\text{ZrO}_2$  as a support for  $\text{ZrO}_2$  (M- $\text{ZrO}_2$ ), in which M = Zr, Y, La, Ca, and Mg. The surface areas of  $\text{TiO}_2$  and Zr- $\text{ZrO}_2$  have been reported to be 146 and  $82 \text{ m}^2 \text{g}^{-1}$ , respectively. Following metal adsorption, the surface area of Co- $\text{TiO}_2$  increased to  $309.8 \text{ m}^2 \text{g}^{-1}$ , while the surface area of La- $\text{ZrO}_2$  increased to  $130 \text{ m}^2 \text{g}^{-1}$ . The observed increase in the surface area may be attributed to the addition of a small amount of metal cations to the support, which improves the structural stability of the catalyst.<sup>68–71</sup>

### 3.6. X-ray photoelectron spectroscopy (XPS)

X-ray photoelectron spectroscopy (XPS) analysis was conducted to investigate the surface composition and chemical states of the synthesized  $\text{Fe}_3\text{O}_4@\text{SiO}_2/\text{Co-Cr-B}$  catalyst.

To investigate the surface electronic states of the synthesized catalyst, XPS analysis was performed using a PHI 5000 Versa Probe spectrometer equipped with a monochromatic Al K $\alpha$  X-ray source ( $h\nu = 1486.6 \text{ eV}$ ). The catalyst powders were gently ground and uniformly distributed onto copper (Cu) substrates, which were used as sample holders for analysis. To minimize the uncontrolled adsorption of atmospheric contaminants, such as water vapor, hydrocarbons, and oxygen, the samples were immediately transferred to a vacuum desiccator after mounting and stored under dry nitrogen conditions. All handling steps prior to the XPS analysis were carried out in a clean, controlled environment to limit exposure to ambient air. The sample transfer into the analysis chamber was performed rapidly to further reduce the possibility of contamination. The spectrometer was operated under ultra-high vacuum conditions ( $\sim 10^{-9}$  mbar) during the measurement. It is important to note that any Cu-related peaks in the spectra may originate from the underlying substrate and were carefully considered during the process of spectral deconvolution and interpretation.

This technique provided critical insights into the successful incorporation of key elements, as confirmed by the general XPS spectrum in Fig. 6-a, which revealed the presence of Si, O, Co, Cr, and B. To gain a detailed understanding of the chemical state of each element, the XPS peaks were deconvoluted using Gaussian functions.

The high-resolution XPS spectrum of Si, shown in Fig. 6-b, highlights a peak at a binding energy of 102.5 eV related to Si-O

bonding, which splits into  $2\text{P}_{1/2}$ , consistent with the presence of  $\text{SiO}_2$  on the surface of the catalyst.<sup>72</sup> Splitting into  $2\text{P}_{1/2}$  is a characteristic feature of the  $\text{SiO}_2$  structure, confirming the chemical state of silicon in the form of silicon dioxide.<sup>73</sup>

Similarly, Fig. 6-c illustrates the high-resolution B 1s spectrum, which reveals two distinct peaks, with the first attributed to the B-O bond with a binding energy of 192.5 eV indicative of boron oxide species,<sup>74</sup> and the second peak centered at 188 eV corresponding to elemental boron or boron in a lower oxidation state, which may be indicative of unoxidized boron or boron carbide structures (B-sub-C).<sup>75</sup> The B 1s binding energy observed near 198 eV is characteristic of boron in tetrahedral coordination, typically associated with  $\text{BO}_4$  units.<sup>76</sup>

The analysis of the C 1s spectrum, shown in Fig. 6-d, further complements these results by exhibiting a strong peak at 284.0 eV, indicative of C-C bonding. This observation aligns well with the previously reported FTIR results, which also confirm the presence of such bonding structures.<sup>77</sup>

In the XPS spectrum of O 1s (Fig. 6-e), a prominent peak at a binding energy of 532.8 eV was detected, which corresponds to C-OH and C=O bonding. This observation is consistent with the presence of hydroxyl groups on the surface, as reported in the FTIR analysis, where -OH groups were identified on the surfaces through XPS analysis.<sup>78</sup>

As shown in Fig. 6-f, the high-resolution Cr 2p spectrum exhibited two characteristic main peaks. The first peak with a binding energy of 576.0 eV corresponds to Cr  $2\text{p}_{3/2}$ , while the second at 586 eV corresponds to Cr  $2\text{p}_{1/2}$ .<sup>79</sup>

The high-resolution XPS spectrum of Co 2p (Fig. 6-g) displays two prominent peaks: one at 781.6 eV, corresponding to Co  $2\text{p}_{3/2}$ , and another at 797.1 eV, assigned to Co  $2\text{p}_{1/2}$ , both of which are characteristic of the  $\text{Co}^{3+}$  oxidation state. The presence of  $\text{Co}^{3+}$  is particularly significant, as it is commonly associated with enhanced catalytic activity due to its ability to facilitate electron transfer processes, which are essential for catalytic reactions such as  $\text{NaBH}_4$  hydrolysis.<sup>6</sup>

However, the reported binding energies can be attributed to various oxides such as  $\text{Co}_3\text{O}_4$ , as reported in the XRD analysis.<sup>64</sup> There are further signature shakeup satellite peaks at 786.0 eV and 803.1 eV that are designated as “sat”, which further supports the presence of cobalt in the catalyst.<sup>80,81</sup>

Atomic percentages were calculated by numerically integrating the intensity over the binding energy using the trapezoidal method. Each elemental peak was approximated using raw intensity data extracted from the XPS spectra. The integrated areas were then normalized to the total signal to derive the atomic percentage of each element (Table 2).

## 4. Parameter's effect

### 4.1. Effect of $\text{Fe}_3\text{O}_4@\text{SiO}_2/\text{Co-Cr}$ ratios on $\text{NaBH}_4$ hydrolysis

In this study, a series of  $\text{Fe}_3\text{O}_4@\text{SiO}_2/\text{Co-Cr-B}$  catalysts were synthesized with varying Co-Cr compositions of 5, 10, 15, 20, 30, and 40% to evaluate their catalytic performance in the hydrolysis of  $\text{NaBH}_4$ . The optimal Cr fraction ( $\chi_{\text{Cr}}$ ) was derived





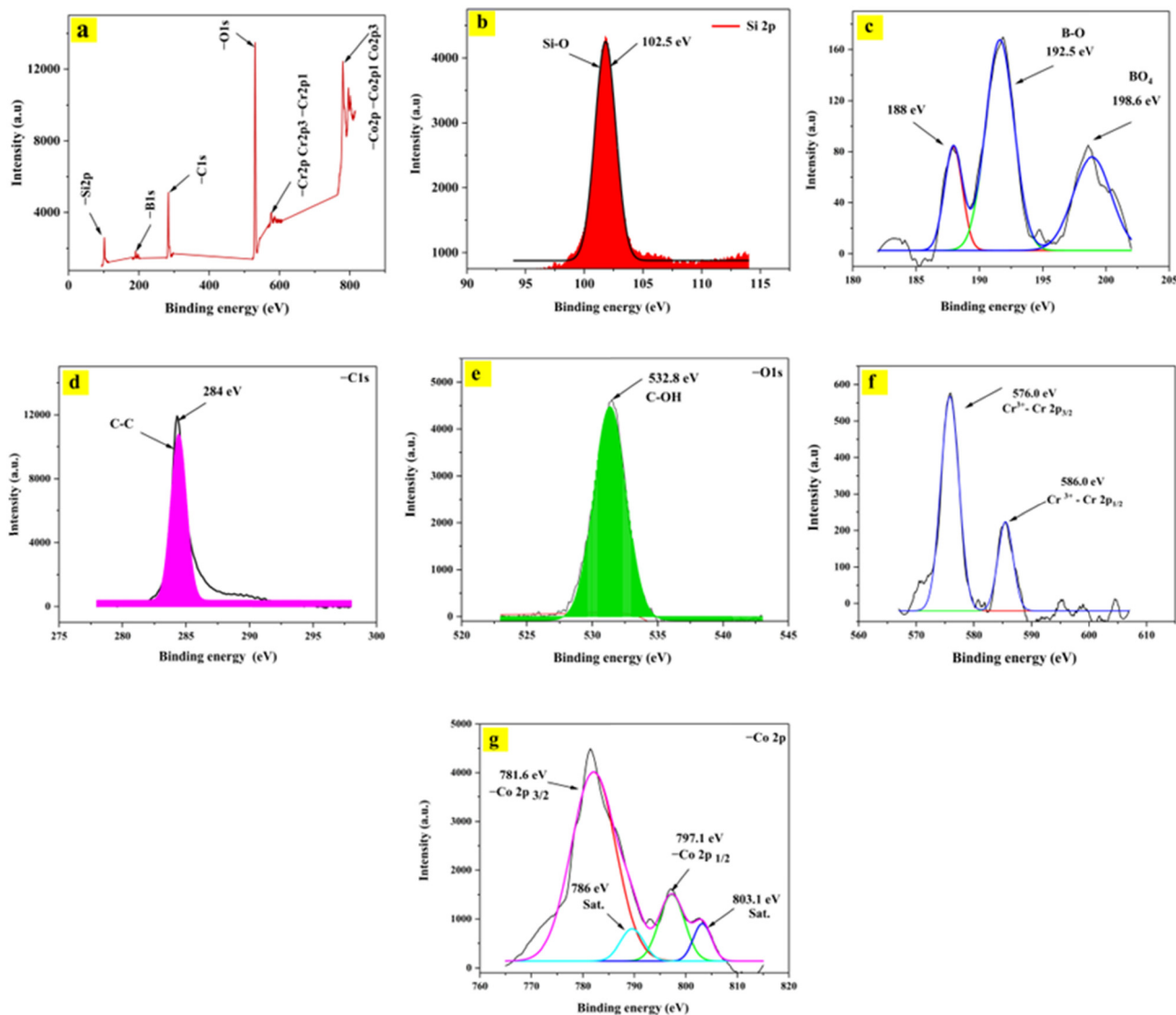


Fig. 6 XPS spectrum of (a) the synthesized catalyst, (b) Si 2p, (c) B 1s, (d) C 1s, (e) O 1s, (f) Cr 2p and (g) Co 2p.

**Table 2** Summary of XPS results: binding energy (eV), assigned species, and atomic percentage (%) of elements in the  $\text{Fe}_3\text{O}_4/\text{SiO}_2\text{-Co-Cr-B}$  catalyst

Element	Binding energy (eV)	Assigned species	Atomic percentage (%)
Si 2p	102.5	Si-O ( $\text{SiO}_2$ )	~ 6.4
B 1s	192.5/188.0	B-O/elemental B	~ 3.7
C 1s	284.0	C-C	~ 22.5
O 1s	532.8	C-OH, C=O	~ 39.2
Cr 2p	576.0/586.0	$\text{Cr}^{3+}$ (Cr 2p <sub>3/2</sub> , 2p <sub>1/2</sub> )	~ 4.9
Co 2p	781.6/797.1	$\text{Co}^{3+}$ (Co 2p <sub>3/2</sub> , 2p <sub>1/2</sub> )	~ 7.8
Co 2p (sat)	786.0/803.1	Satellite peaks ( $\text{Co}^{3+}$ )	~ 7.8

from the literature and defined as  $\chi_{\text{Cr}} = \text{Cr}/(\text{Co} + \text{Cr}) = 4\%$ .<sup>63</sup> The reactions were conducted in the presence of 1%  $\text{NaBH}_4$  and 7%  $\text{NaOH}$  at 30 °C using 100 mg of catalyst.

The optimized catalyst was synthesized with a targeted Cr:Co atomic doping ratio of 4:96, corresponding to a molar ratio

of approximately 0.042. This intended composition was confirmed by energy-dispersive X-ray spectroscopy (EDX), which measured Cr and Co contents of 0.74 wt% and 14.84 wt%, respectively. These values yielded a Cr:Co weight ratio of approximately 0.049, which aligns well with the designed atomic ratio when considering the relative atomic weights of Cr and Co.

As shown in Fig. 7, for 5% (Co-Cr) the HGR was  $3.36 \text{ L g}_{\text{metal}}^{-1} \text{ min}^{-1}$ , with the required hydrogen volume being achieved within 23 min. An increase in the Co-Cr content from 10 to 30% led to a significant enhancement in the hydrogen generation rate (HGR) from  $12.21 \text{ L g}_{\text{metal}}^{-1} \text{ min}^{-1}$  to  $22.2 \text{ L g}_{\text{metal}}^{-1} \text{ min}^{-1}$ . However, at 40% (Co-Cr), the HGR decreased to  $13.58 \text{ L g}_{\text{metal}}^{-1} \text{ min}^{-1}$ .

This observed situation can be attributed to several factors. The addition of chromium (Cr) as a dopant in Co-based catalysts has been shown to significantly enhance hydrogen generation rates, with improvements reaching up to 3–4 times that of undoped catalysts.



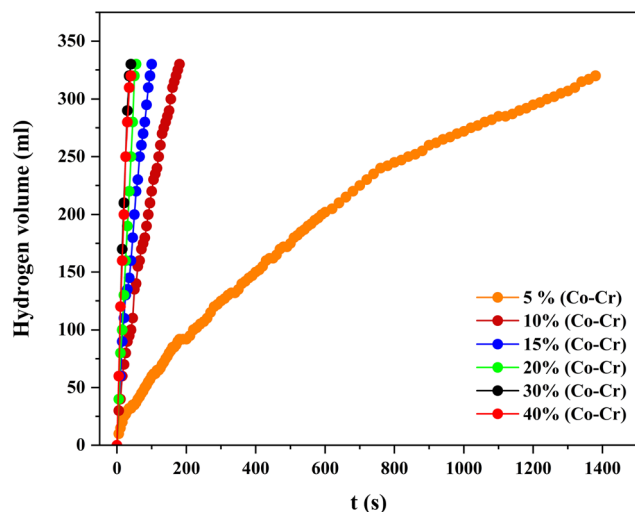


Fig. 7 The hydrogen volume variation with Co–Cr% (7% NaOH, 30 °C, 100 mg catalyst, 1% NaBH<sub>4</sub>).

Cr promotes the formation of chromium oxide on the catalyst surface, as evidenced by XRD analysis, which confirms the presence of Cr<sub>2</sub>O<sub>3</sub> and Cr<sub>2</sub>O<sub>4</sub> phases. These oxides play a critical role in improving the dispersion of Co-based particles, such as Co–B, by preventing particle agglomeration and increasing the active surface area, ensuring greater accessibility to catalytic sites.

Additionally, Cr introduces Lewis acid sites into the catalyst, enhancing the adsorption and activation of OH<sup>−</sup> ions – key intermediates in the NaBH<sub>4</sub> hydrolysis reaction – thereby accelerating the reaction kinetics. Furthermore, Cr strengthens the electronic interactions with Co, optimizes the charge transfer processes, and boosts the catalytic efficiency. These effects are further amplified when Cr is combined with other transition metals, such as tungsten (W), molybdenum (Mo), or copper (Cu), which collectively contribute to an expanded active surface area and improved catalytic performance.

Collectively, these findings emphasize the pivotal role of Cr in enhancing the catalytic performance of Co-based systems for hydrogen generation. Moreover, for effective NaBH<sub>4</sub> hydrolysis, the ideal Co–Cr ratio (30%) probably strikes a balance between sufficient active sites and the required electrical interactions. This is consistent with the general finding that by maximizing the surface shape and electrical characteristics, certain metal ratios can enhance the catalytic performance.<sup>63,82</sup>

Among the synthesized catalysts, the Fe<sub>3</sub>O<sub>4</sub>@SiO<sub>2</sub>/30%(Co–Cr) composition was identified as the optimal loading for the NaBH<sub>4</sub> hydrolysis reaction.

#### 4.2. Effect of sodium hydroxide (NaOH) concentration on NaBH<sub>4</sub> hydrolysis

The effect of NaOH concentration on the hydrogen generation rate (HGR) was studied through experiments carried out with different concentrations of NaOH (3, 5, 7, and 10%). All the experiments were conducted at a process temperature of 30 °C using 1% NaBH<sub>4</sub> and 100 mg of the catalyst.

NaOH is commonly used as a stabilizer to prevent the self-hydrolysis of NaBH<sub>4</sub> when it is dissolved in distilled water.<sup>83,84</sup>

As shown in Fig. 8, increasing the NaOH concentration from 3% to 7% resulted in a significant increase in the HGR from 19.14 L g<sub>metal</sub><sup>−1</sup> min<sup>−1</sup> to 22.2 L g<sub>metal</sub><sup>−1</sup> min<sup>−1</sup>.

This increase may be due to the addition of hydroxyl ions (OH<sup>−</sup>) to the reaction medium, which changes the electronic properties of the catalyst, thereby enhancing the substrate–catalyst interaction, resulting in the release of more hydrogen.<sup>52</sup> However, with a further increase in NaOH concentration (10%), the HGR decreased to 21.07 L g<sub>metal</sub><sup>−1</sup> min<sup>−1</sup>. This decrease can be explained by the increased viscosity of the solution caused by excess hydroxyl ions (OH<sup>−</sup>), resulting in a decrease in the diffusion rate, which inhibits hydrogen generation.<sup>83</sup>

OH<sup>−</sup> ions can be competitively adsorbed on the catalyst surface with respect to BH<sup>+</sup> ions, ultimately decreasing the HGR.<sup>85</sup> Furthermore, a higher NaOH concentration facilitates the formation of by-products, such as NaBO<sub>2</sub>·xH<sub>2</sub>O and NaB(OH)<sub>4</sub>, which are deposited on the surface of the catalyst, inhibiting hydrogen release.<sup>86</sup>

The presence of –OH groups on the catalyst support plays a pivotal role in enhancing the metal–support interaction, which is essential for the uniform dispersion of active metal sites such as Pt. This enhanced dispersion increases the availability of catalytic sites, resulting in a higher hydrogen generation rate (HGR) and reduced activation energy during the hydrolysis process.

Additionally, –OH groups contribute to improved electronic conductivity by creating electron-enriched active sites, which facilitate charge transfer and accelerate reaction kinetics. These combined effects highlight the crucial role of –OH groups in enhancing the catalytic performance for hydrogen generation.<sup>87</sup>

However, for the next stages, 7% NaOH was tallied as a suitable concentration.

#### 4.3. Effect of catalyst amount on NaBH<sub>4</sub> hydrolysis

The effect of catalyst amount on hydrogen generation was examined by varying the catalyst amount to 25, 50, 75, and 100 mg in the presence of 1% NaBH<sub>4</sub> and 7% NaOH at 30 °C.

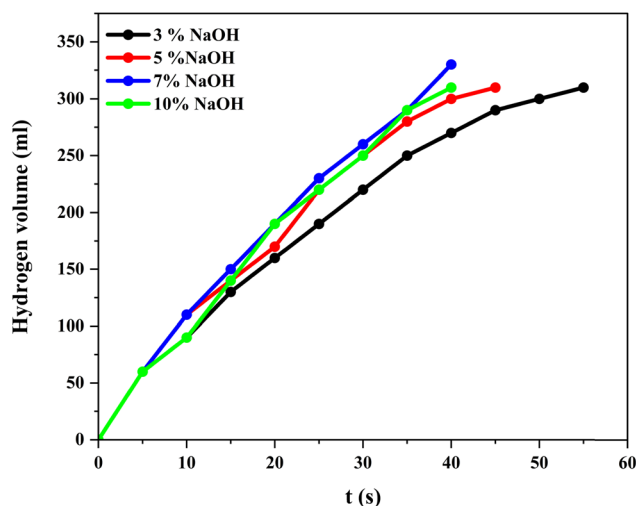


Fig. 8 Hydrogen volume variation with NaOH concentration (1% NaBH<sub>4</sub>, 100 mg catalyst, 30 °C).



As shown in Fig. 9, increasing the catalyst amount from 25 mg to 100 mg resulted in a substantial decrease in reaction time and a significant increase in the hydrogen generation rate (HGR), which increased from  $13.24 \text{ L g}_{\text{metal}}^{-1} \text{ min}^{-1}$  to  $22.2 \text{ L g}_{\text{metal}}^{-1} \text{ min}^{-1}$ .

This enhancement can be attributed to the increased number of active sites as the catalyst amount increased, which accelerated the reaction and boosted hydrogen generation efficiency.<sup>88–90</sup>

As highlighted in the FESEM image (Fig. 2-e), spherical particles, such as those observed in the  $\text{NiFe}_2\text{O}_4$  and  $\text{Co}_3\text{O}_4$  catalysts, have been shown to optimize catalytic performance by providing a uniform surface area that enhances reaction kinetics and stability.<sup>91,92</sup>

The spherical shape facilitates better contact with the reactants, thereby improving the efficiency of hydrogen generation. Moreover, spherical particles often have a higher surface-area-to-volume ratio, which increases the number of active sites available for the reaction. This is crucial for enhancing the hydrogen generation rate because more active sites can facilitate faster reaction rates.<sup>93,94</sup> The uniformity of spherical particles aids in better heat and mass transfer during the reaction, which is essential for maintaining optimal reaction conditions and improving the overall hydrogen generation rate.<sup>95</sup>

The surface composition and chemical states of the  $\text{Fe}_3\text{O}_4@\text{-SiO}_2/\text{Co-Cr-B}$  catalyst, as revealed by XPS analysis, play a critical role in the effect of catalyst amount on  $\text{NaBH}_4$  hydrolysis.

The  $\text{SiO}_2$  support, evidenced by the Si 2p and O 1s states, prevents the aggregation of Co-B nanoclusters, thereby maintaining a high surface area and enhancing catalytic activity through improved reaction kinetics.<sup>65</sup> Co 2p states indicate the presence of both elemental and oxidized forms of Co, which facilitate electron transfer and strengthen the electronic interactions with B and Cr, further boosting catalytic performance.<sup>63,65</sup>

Similarly, Cr 2p states reveals the dual role of Cr in the system: at optimal concentrations, Cr enhances the dispersion of Co-B particles and increases the surface area, significantly improving catalytic activity. However, excessive Cr leads to the formation of surface oxides that block active sites, thereby reducing efficiency.<sup>65,96</sup> These findings highlight the importance of optimizing surface composition and chemical states to maximize the catalyst's performance in  $\text{NaBH}_4$  hydrolysis. In the following step of the study, parameter impacts were investigated using 100 mg of catalyst.

Fig. 9 also shows the change in  $\ln(\text{HGR})$  with  $\ln(\text{catalyst amount})$ , which fluctuates linearly with  $\ln(\text{catalyst amount})$ , in order to ascertain the relationship between the reaction rate and catalyst amount. This finding indicates that depending on the catalyst amount, the hydrolysis process was approximately first order ( $n = 0.982$ ).

#### 4.4. Effect of sodium borohydride ( $\text{NaBH}_4$ ) on $\text{NaBH}_4$ hydrolysis

The effect of  $\text{NaBH}_4$  concentration on  $\text{NaBH}_4$  hydrolysis was studied at 1, 3, 5, and 7%  $\text{NaBH}_4$  using 100 mg of the catalyst and 7%  $\text{NaOH}$  at  $30^\circ\text{C}$ . As illustrated in Fig. 10, as  $\text{NaBH}_4$

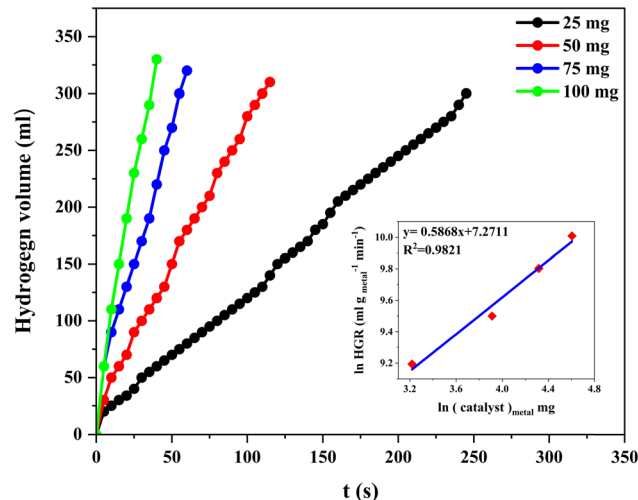


Fig. 9 The hydrogen volume variation with the catalyst amount (1%  $\text{NaBH}_4$ , 7%  $\text{NaOH}$ ,  $30^\circ\text{C}$ ).

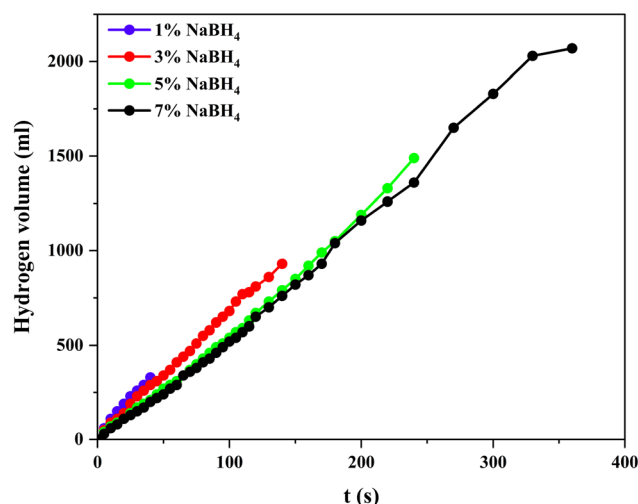


Fig. 10 The hydrogen volume variation with  $\text{NaBH}_4$  concentration (100 mg catalyst, 7%  $\text{NaOH}$ ,  $30^\circ\text{C}$ ).

concentration increased from 1% to 5%, the HGR decreased from  $22.2 \text{ L g}_{\text{metal}}^{-1} \text{ min}^{-1}$  to  $11.52 \text{ L g}_{\text{metal}}^{-1} \text{ min}^{-1}$ . Further increases in  $\text{NaBH}_4$  concentration, up to 7%, resulted in a slight reduction of the HGR to  $11.47 \text{ L g}_{\text{metal}}^{-1} \text{ min}^{-1}$ .

The hydrolysis reaction in the liquid phase proceeds *via* two critical steps.

1. Equilibrium adsorption of  $\text{BH}_4^-$  species on the catalyst surface.
2. Hydrogen generation from adsorbed species.<sup>97</sup>

As  $\text{NaBH}_4$  concentration increases, the viscosity of the solution also increases, leading to the precipitation of  $\text{NaBO}_2$  by-products on the catalyst surface. This precipitation impairs hydrogen generation by obstructing the active sites. Additionally, increased viscosity inhibits mass transfer, further decreasing the overall catalytic performance.<sup>98,99</sup> Moreover, the interaction of functional groups with  $\text{NaBH}_4$  molecules, as





observed in the FTIR analysis, is pivotal in determining the efficiency of hydrogen generation. The C–O and C=O groups can facilitate the adsorption of NaBH<sub>4</sub> onto the catalyst surface, promoting its decomposition and subsequent hydrogen release. This is because these groups can form hydrogen bonds or other interactions with NaBH<sub>4</sub>, stabilizing the transition state and lowering the activation energy required for the reaction.<sup>100</sup> Additionally, the presence of C–OH groups can further enhance these interactions by providing additional sites for NaBH<sub>4</sub> adsorption and activation.

#### 4.5. Effect of temperature on NaBH<sub>4</sub> hydrolysis

To understand the effect of temperature on the hydrolysis reaction, experiments were carried out at different temperatures (20, 30, 40, and 50 °C) in the presence of 7% NaOH, 1% NaBH<sub>4</sub>, and 100 mg of catalyst.

As shown in Fig. 11, the HGR increases from 14.67 L g<sub>metal</sub><sup>−1</sup> min<sup>−1</sup> to 27.51 L g<sub>metal</sub><sup>−1</sup> min<sup>−1</sup> as the temperature increases from 20 °C to 50 °C. This resulted in a significant decrease in the time required for hydrogen generation. Increasing the temperature increased the mobility of the molecules, thereby increasing their collision probability. In addition, the interactions between the catalyst surface and molecules become more intense. This leads to a significant increase in HGR.<sup>101,102</sup>

Table 3 highlights the performance of the polynomial regression model used to analyze the data for all parameters (NaOH concentration, catalyst amount, NaBH<sub>4</sub> concentration, and temperature). The key performance metrics include mean squared error (MSE), standard deviation (*S*), and *R*-squared (*R*<sup>2</sup>) values.

For NaOH concentration, the model explained 99.8% of the variability in HGR (*R*<sup>2</sup> = 0.998), indicating strong predictive capability with minimal error (MSE = 2.31 × 10<sup>3</sup>; *S* = 48.1). In the case of catalyst amount, the model effectively captured nonlinear behavior, reflected in an *R*<sup>2</sup> of 0.976, and a corresponding MSE of 3.39 × 10<sup>5</sup>. Similarly, for NaBH<sub>4</sub> concentration,

**Table 3** Overview of the performance metrics including mean squared error (MSE), standard deviation (*S*), and *R*-squared (*R*<sup>2</sup>) values

Parameter	Mean squared error (MSE)	Standard deviation ( <i>S</i> )	<i>R</i> -squared ( <i>R</i> <sup>2</sup> )
NaOH concentration (wt%)	2.31 × 10 <sup>3</sup>	4.81 × 10 <sup>1</sup>	0.998
Catalyst amount (mg)	3.39 × 10 <sup>5</sup>	5.82 × 10 <sup>2</sup>	0.976
NaBH <sub>4</sub> concentration (wt%)	2.48 × 10 <sup>5</sup>	4.98 × 10 <sup>2</sup>	0.987
Temperature (°C)	2.24 × 10 <sup>5</sup>	4.73 × 10 <sup>2</sup>	0.991

the polynomial regression yielded robust performance (*R*<sup>2</sup> = 0.987; MSE = 2.48 × 10<sup>5</sup>). Regarding temperature, the model demonstrated the highest predictive accuracy, with an *R*<sup>2</sup> of 0.991 and the lowest MSE (2.24 × 10<sup>5</sup>).

However, it is important to note that the turnover frequency (TOF) was calculated based on a single experimental condition (7 wt% NaOH, 1 wt% NaBH<sub>4</sub>, and 30 °C). Therefore, no statistical averaging or error analysis can be applied to TOF in this context.

#### 4.6. Kinetic study

Experimental data from the catalytic hydrolysis of NaBH<sub>4</sub> using the Fe<sub>3</sub>O<sub>4</sub>@SiO<sub>2</sub>/Co–Cr–B catalyst at various temperatures were employed to conduct kinetic analyses. Both the *n*th-order and Langmuir–Hinshelwood kinetic models were applied to evaluate the reaction kinetics of hydrogen generation from NaBH<sub>4</sub> hydrolysis.

The rate constant *k* and the activation energy can be calculated according to eqn (2):

$$-r_{\text{NaBH}_4} = -\frac{dC_{\text{NaBH}_4}}{dt} = k \cdot C_{\text{NaBH}_4}^n \quad (2)$$

By integrating over time and concentration, we obtain

$$-\int_{C_{\text{NaBH}_4,0}}^{C_{\text{NaBH}_4}} \frac{dC_{\text{NaBH}_4}}{C_{\text{NaBH}_4}^n} = k \int_0^t dt \quad (3)$$

Finally, we get

$$\frac{1}{C_{\text{NaBH}_4}^{n-1}} = (n-1) \cdot k \cdot t + \frac{1}{C_{\text{NaBH}_4,0}^{n-1}} \quad (4)$$

The Arrhenius equation was used to calculate the activation energy of the NaBH<sub>4</sub> hydrolysis reaction (eqn (5)):

$$\ln k = \ln A - \frac{E_a}{RT} \quad (5)$$

In addition, the activation energy can be determined from the slope of the 1/*T* ~ ln *k* graph (Fig. 12-a).

According to the results, the activation energy was determined as 20.75 kJ mol<sup>−1</sup>.

#### 4.7. Langmuir–Hinshelwood kinetic model

The Langmuir–Hinshelwood model is widely used to determine the activation energy:

$$\frac{dC_{\text{NaBH}_4}}{dt} = -r \cdot \text{NaBH}_4 = -k \frac{k_a C_{\text{NaBH}_4}}{1 + k_a C_{\text{NaBH}_4}} \quad (6)$$

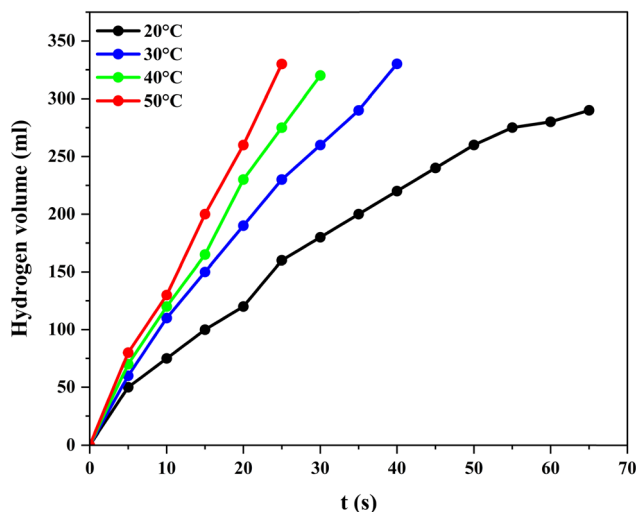


**Fig. 11** The hydrogen volume variation with temperature (1% NaBH<sub>4</sub>, 7% NaOH, 100 mg catalyst).



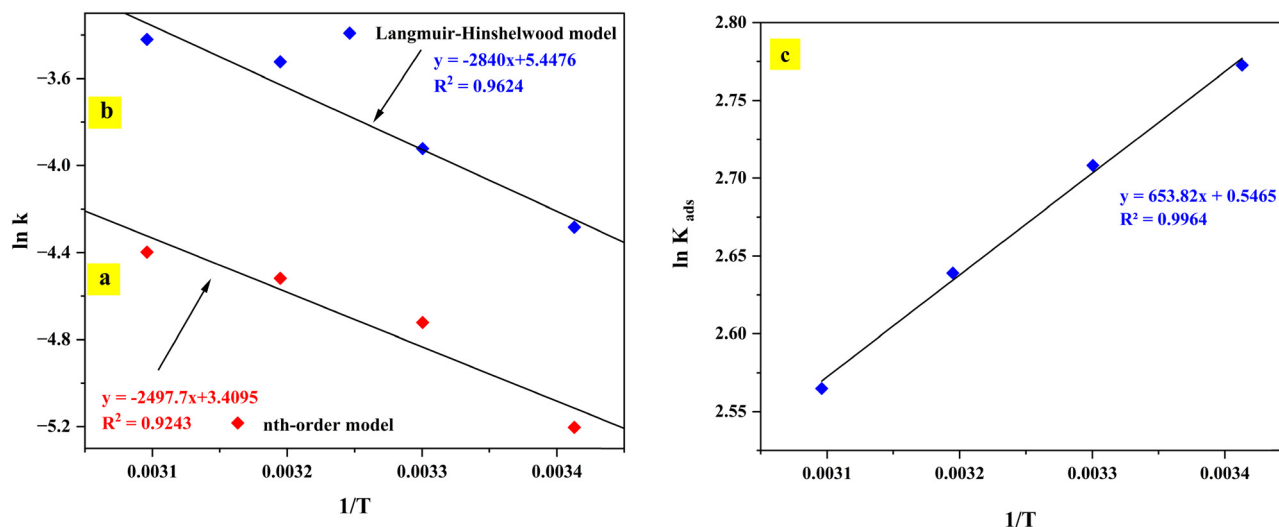


Fig. 12 (1/T) variation with  $\ln(k)$  for  $\text{NaBH}_4$  hydrolysis for the (a)  $n$ th-order model and (b) Langmuir–Hinshelwood model. (c) (1/T) variation with  $\ln K_{\text{ads}}$ .

By integrating we obtain eqn (7), which allows us to calculate the activation energy:

$$\frac{1}{k_a} \cdot \ln \frac{\text{NaBH}_4}{\text{NaBH}_4} + \text{NaBH}_4 - \text{NaBH}_4 = -kt \quad (7)$$

From the (1/T) vs  $\ln(k)$  graph (Fig. 12-b), the activation energy was determined as  $23.60 \text{ kJ mol}^{-1}$ .

To enhance the interpretation of the temperature-dependent adsorption behavior, a thermodynamic analysis was conducted using the van't Hoff equation.

However, eqn (8) can be used to compute the entropy change ( $\Delta S^\circ$ ) and enthalpy change ( $\Delta H_{\text{ads}}$ ) based on the obtained  $K_{\text{ads}}$  values. From this, it is also possible to calculate the Gibbs free energy change ( $\Delta G^\circ$ ).

$$\ln K_{\text{ads}} = \frac{\Delta S^\circ}{R} - \frac{\Delta H_{\text{ads}}}{R} \frac{1}{T} \quad (8)$$

A linear correlation was observed in the van't Hoff plot of  $\ln(K_{\text{ads}})$  versus  $1/T$ , indicating that the adsorption process adheres to classical thermodynamic expectations. From the slope and intercept of the regression line in Fig. 12-c, the standard enthalpy change of adsorption ( $\Delta H^\circ$ ) was calculated to be  $-5.44 \text{ kJ mol}^{-1}$ , confirming the exothermic nature of the adsorption process. The corresponding standard entropy change ( $\Delta S^\circ$ ) was determined to be  $+4.54 \text{ J mol}^{-1} \text{ K}^{-1}$ , suggesting a modest increase in system disorder upon adsorption.

Furthermore, the standard Gibbs free energy change ( $\Delta G^\circ$ ) (eqn (9)) was computed over the investigated temperature range, yielding values from  $-6.76 \text{ kJ mol}^{-1}$  at 293 K to  $-6.90 \text{ kJ mol}^{-1}$  at 323 K:

$$\Delta G^\circ = \Delta H_{\text{ads}} - T \cdot \Delta S^\circ \quad (9)$$

These negative  $\Delta G^\circ$  values indicate that the adsorption remains thermodynamically spontaneous across all studied temperatures. However, the diminishing magnitude of  $\Delta G^\circ$  with increasing temperature aligns with the observed decrease

in the adsorption constant ( $K_{\text{ads}}$ ), attributable to enhanced desorption kinetics. This analysis reinforces the mechanistic conclusion that temperature-induced desorption is the primary factor governing the decline in adsorption capacity at elevated temperatures.

Nevertheless, the Gibbs free energy change ( $\Delta G^\circ$ ) at each temperature can also be determined using eqn (9) and is summarized in Table 4.

The fit of the experimental data to the Langmuir–Hinshelwood kinetic model was rigorously evaluated across a range of temperatures (20–50 °C) and corresponding concentration variations. The model exhibited excellent agreement with the experimental results at all temperatures, as indicated by the high coefficients of determination ( $R^2$ ) of 0.998 at 20 °C, 0.9994 at 30 °C, 0.9966 at 40 °C, and 0.9976 at 50 °C. These  $R^2$  values suggest a strong correlation between the model predictions and observed data, supporting the applicability of the Langmuir–Hinshelwood model under the studied conditions.

Further statistical validation was conducted by calculating the mean squared error (MSE) and the standard deviation ( $S$ ) of the experimental concentrations. At 20 °C, MSE was notably low at  $8.0 \times 10^{-6}$ , with a standard deviation of 0.07599. At 30 °C, MSE increased slightly to 0.00248, accompanied by a standard deviation of 0.07069. At 40 and 50 °C, the MSE values were 0.00339 and 0.00393, respectively, with the corresponding standard deviations of 0.07779 and 0.08571, respectively. These

Table 4 Overview of the  $\Delta G^\circ$ ,  $\Delta S^\circ$ , and  $\Delta H_{\text{ads}}$  values derived from  $K_{\text{ads}}$  calculations

$T$	$K_{\text{ads}}$	$\Delta G^\circ$ ( $\text{kJ mol}^{-1}$ )	$\Delta S^\circ$ ( $\text{J mol}^{-1} \text{ K}^{-1}$ )	$\Delta H_{\text{ads}}$ ( $\text{kJ mol}^{-1}$ )
20 °C	16	−6.67	$4.54 \pm 0.01$	$-5.44 \pm 0.01$
30 °C	15	−6.81		
40 °C	14	−6.85		
50 °C	13	−6.90		



relatively low MSE values across all temperatures demonstrated a consistently strong fit of the model, whereas the standard deviations reflected reasonable variability within the experimental data, which is typical for catalytic kinetic systems.

In addition to the goodness-of-fit metrics, the kinetic parameters derived from model fitting, including the rate constant ( $k$ ) and adsorption constant ( $K$ ), also showed logical trends with temperature. The rate constant increased from 0.0077 at 20 °C to 0.0173 at 50 °C, indicating an acceleration of the reaction kinetics with temperature, as expected from Arrhenius-type behavior.

Conversely, the adsorption constant ( $K$ ) decreased from 16 to 13 over the same temperature range, which is consistent with the reduced surface adsorption at elevated temperatures owing to enhanced desorption dynamics. However, the absorption equilibrium constant ( $K_{\text{ads}}$ ) measures the similarity between the adsorbate and adsorbent systems, and a higher  $K_{\text{ads}}$  value often indicates greater adsorption effectiveness of inhibitor molecules on the metallic surface.

Collectively, the combination of high  $R^2$  values, low MSEs, and reasonable trends in the kinetic parameters confirmed that the Langmuir–Hinshelwood model not only fits the experimental data well across the investigated conditions but also yields statistically robust and physically meaningful parameters (Table 5).

The typical decrease in the adsorption constant ( $K$ ) with increasing temperature is primarily due to enhanced desorption kinetics. As the temperature increased, the adsorbed species gained more thermal energy, making it easier for them to overcome the adsorption energy barrier and desorb from the surface. This leads to reduced surface coverage and a lower value of  $K$ . This behavior is characteristic of exothermic adsorption processes, where equilibrium shifts toward desorption at higher temperatures.<sup>103–105</sup>

In heterogeneous catalysis, turnover frequency (TOF) is a crucial kinetic parameter that shows how many reactant

molecules are transformed per active site in a certain amount of time. It is commonly represented as  $\text{mol}_{\text{H}_2} \text{mol}_{\text{cat}}^{-1} \text{h}^{-1}$ , as eqn (10) illustrates. TOF concentrates on the number of active sites engaged in the reaction, as opposed to the hydrogen generation rate (HGR), which counts the quantity of hydrogen generated in relation to the mass of the catalyst. Through this process of normalizing catalytic activity, TOF offers a clear indicator of intrinsic efficiency that is unaffected by changes in mass, surface area, or catalyst loading.<sup>106–108</sup>

$$\text{Turnover frequency (mol}_{\text{H}_2} \text{mol}_{\text{cat}}^{-1} \text{h}^{-1}) = \frac{n_{\text{mol}_{\text{H}_2}}}{\text{catalyst}_{\text{mol}} \text{time}_{\text{h}}} \quad (10)$$

At 30 °C, the  $\text{Fe}_3\text{O}_4@\text{SiO}_2/\text{Co-Cr-B}$  catalyst exhibited a remarkable turnover frequency (TOF) of  $2110.61 \text{ mol}_{\text{H}_2} \text{mol}_{\text{cat}}^{-1} \text{h}^{-1}$  during  $\text{NaBH}_4$  hydrolysis, corresponding to a hydrogen generation rate (HGR) of  $22.2 \text{ L g}_{\text{metal}}^{-1} \text{min}^{-1}$ .

Table 6 compares the activation energy and HGR of the  $\text{Fe}_3\text{O}_4@\text{SiO}_2/\text{Co-Cr-B}$  catalyst with those of other Co, Cr, and  $\text{Fe}_3\text{O}_4@\text{SiO}_2$  catalysts reported in the literature. Notably, our catalyst exhibited a high hydrogen generation rate with very low activation energy.

To contextualize the catalytic performance of the synthesized  $\text{Fe}_3\text{O}_4@\text{SiO}_2/\text{Co-Cr-B}$  catalyst, a benchmark comparison was performed with several state-of-the-art non-noble metal catalysts reported in the literature, as well as our previously developed  $\text{IA-CNT}@\text{Co-Mo-B}$  catalyst. The  $\text{Fe}_3\text{O}_4@\text{SiO}_2/\text{Co-Cr-B}$  catalyst demonstrated a hydrogen generation rate (HGR) of  $22.20 \text{ L min}^{-1} \text{g}^{-1}$  and a low activation energy ( $E_a$ ) of  $23.60 \text{ kJ mol}^{-1}$ , both of which significantly exceed the performance metrics of many reported systems.

Compared to our previously synthesized  $\text{IA-CNT}@\text{Co-Mo-B}$ , which achieved an HGR of  $5.3 \text{ L min}^{-1} \text{g}^{-1}$  and an  $E_a$  of  $24.58 \text{ kJ mol}^{-1}$ , the  $\text{Fe}_3\text{O}_4@\text{SiO}_2/\text{Co-Cr-B}$  catalyst exhibits over a fourfold increase in HGR, while maintaining a slightly lower

**Table 5** Langmuir–Hinshelwood model fitting parameters and statistical metrics at different temperatures

Temperature (°C)	Rate constant ( $k$ )	Adsorption constant ( $K$ )	$R$ -squared ( $R^2$ )	Mean squared error (MSE)	Standard deviation ( $S$ )
20	0.0077	16	0.9980	0.000008	0.075986
30	0.0125	15	0.9994	0.002478	0.070691
40	0.0146	14	0.9966	0.003390	0.077790
50	0.0173	13	0.9976	0.003930	0.085710

**Table 6** Comparison of the catalytic performance of the  $\text{Fe}_3\text{O}_4@\text{SiO}_2/\text{Co-Cr-B}$  catalyst with that of other catalysts for hydrogen generation from  $\text{NaBH}_4$

Catalyst	Experimental conditions	HGR ( $\text{L g}^{-1} \text{min}^{-1}$ )	$E_a$ ( $\text{kJ mol}^{-1}$ )	Ref.
$\text{Ru-Co}_3\text{O}_4$	1 wt% NaOH, 10 wt% $\text{NaBH}_4$	6.51	28.26	13
CNT-promoted Co-B	5 wt% NaOH, 5 wt% $\text{NaBH}_4$	12.00	23.5	109
Amorphous Co-Cr-B	1 mol NaOH/L, 1 mol $\text{NaBH}_4$ /L	0.11	44.51	96
Co-P-B	2.5 M NaOH, 0.025 M $\text{NaBH}_4$	4	32	110
Carbon-supported Co-B	20 mM NaOH, 0.2 M $\text{NaBH}_4$	2.07	57.8	111
Ni-B-Cr0.8@RH	1.25 wt% NaOH, 2.5 wt% $\text{NaBH}_4$	1.42	50.64	112
Co-Cr-B@NG	1.0 wt% NaOH, 1.5 wt% $\text{NaBH}_4$	2.23	38.41	113
Co-B/HPCM	5 wt% NaOH, 2.25 wt% $\text{NaBH}_4$	3.08	43.3	114
$\text{Fe}_3\text{O}_4@\text{SiO}_2/\text{Co-Cr-B}$	7 wt% NaOH, 1 wt% $\text{NaBH}_4$	22.2	23.6	This study





activation energy. These results suggest a more efficient catalytic pathway and superior hydrogen evolution kinetics under similar experimental conditions.<sup>115</sup>

This performance surpasses that of g-C<sub>3</sub>N<sub>4</sub>/Co-W-B/Ni foam, which exhibited an HGR of 7.3 L min<sup>-1</sup> g<sup>-1</sup> and an  $E_a$  of 31.5 kJ mol<sup>-1</sup>.<sup>116</sup> Additionally, it outperforms the Ni-Co/r-GO catalyst, which achieved a hydrogen production rate of 1.28 L min<sup>-1</sup> g<sup>-1</sup> and a considerably higher  $E_a$  of 55.12 kJ mol<sup>-1</sup>.<sup>117</sup>

The superior HGR and notably lower activation energy of Fe<sub>3</sub>O<sub>4</sub>@SiO<sub>2</sub>/Co-Cr-B highlight its highly efficient catalytic behavior and favorable reaction kinetics. These attributes indicate that the catalyst can effectively initiate and sustain hydrogen generation reactions at lower energy thresholds, which is a key consideration for practical and scalable hydrogen production systems.

#### 4.8. Suggested mechanism for NaBH<sub>4</sub> hydrolysis according to the Langmuir–Hinshelwood model

To understand the reaction order ( $n$ ) changes and activation energy ( $E_a$ ) for a chemical reaction, the Langmuir–Hinshelwood model was suggested. For this purpose, the following procedure (Fig. 13) was proposed to understand the mechanism. Initially, BH<sub>4</sub><sup>-</sup> ions and H<sub>2</sub>O molecules were adsorbed onto the catalyst surface. Subsequently, the adsorbed BH<sub>4</sub><sup>-</sup> ions react with the catalyst surface to release surface-bound hydrogen species. This was followed by adsorption of additional water molecules onto the catalyst surface. The surface-bound hydrogen reacts with the adsorbed water molecules, producing molecular hydrogen (H<sub>2</sub>) and BH<sub>3</sub>(OH)<sup>-</sup> as the reaction products. The desorption of H<sub>2</sub> from the catalyst surface marks the completion of the hydrogen generation step. Finally, the catalyst surface was

regenerated through the desorption of BH<sub>3</sub>(OH)<sup>-</sup> and the adsorption of fresh reactants, allowing the cycle to repeat.

#### 4.9. Fe<sub>3</sub>O<sub>4</sub>@SiO<sub>2</sub>/Co-Cr-B reusability in NaBH<sub>4</sub> hydrolysis

The reusability of the Fe<sub>3</sub>O<sub>4</sub>@SiO<sub>2</sub>/Co-Cr-B catalyst in NaBH<sub>4</sub> hydrolysis is a key factor, as improved reusability enhances the catalyst's stability and durability, thereby minimizing the need for frequent replacement. Reusability experiments were conducted at 30 °C using 1% NaBH<sub>4</sub>, 100 mg of catalyst, and 7% NaOH. After each experiment, the catalyst was dried under N<sub>2</sub> gas at 80 °C for 4 h to prepare for the next cycle.

As depicted in Fig. 14, the hydrogen generation rate (HGR) decreased from 18.80 L g<sub>metal</sub><sup>-1</sup> min<sup>-1</sup> in the first cycle to 4.08 L g<sub>metal</sub><sup>-1</sup> min<sup>-1</sup> after six reaction cycles. This decline in

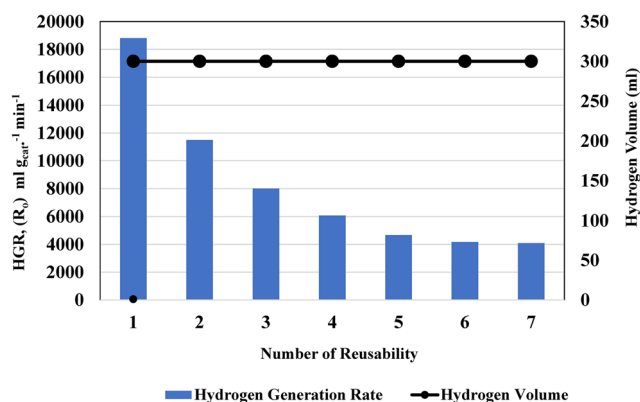


Fig. 14 Hydrogen generation rate variation with the number of reusability (30 °C, 1% NaBH<sub>4</sub>, 100 mg catalyst, 7% NaOH).

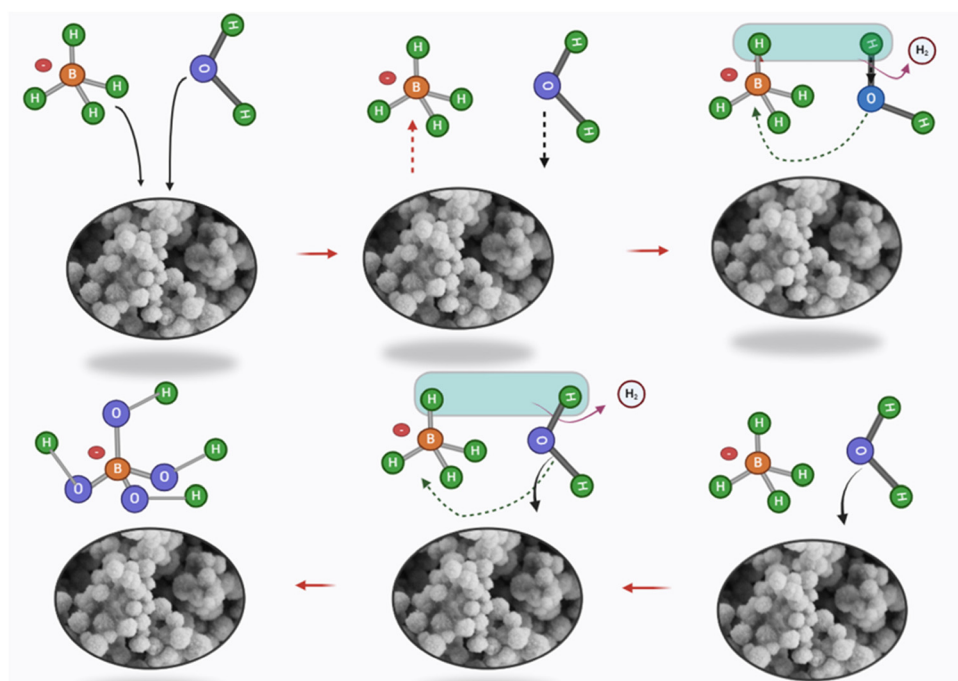


Fig. 13 Suggested mechanism for NaBH<sub>4</sub> hydrolysis according to the Langmuir–Hinshelwood mode.



performance can be attributed either to the loss of approximately 90% of the catalyst during its recovery from the hydrolysis process, or to the precipitation of  $\text{NaBO}_2$  on the catalyst surface, which blocks active sites and reduces hydrogen generation. Despite this, theoretical hydrogen volume was achieved in each reusability experiment, indicating that the catalyst maintained its hydrogen generation potential, even after repeated use.<sup>118</sup>

FE-SEM analysis revealed that the catalyst maintained its spherical morphology with no significant structural alterations after the reusability experiments, indicating good morphological stability under the applied conditions, which is consistent with previous reports (Fig. 15-a and -c). However, EDX analysis confirmed the presence of borate species on the catalyst surface, suggesting that surface interactions or deposition occurred during the reaction.<sup>119,120</sup> Moreover, inductively coupled plasma (ICP) analysis revealed that the catalyst retained its elemental integrity over five consecutive hydrolysis cycles with no detectable leaching of Co or Cr into the reaction medium. This confirmed the excellent compositional stability and reusability of the catalyst under the applied conditions.

## 5. Conclusions

In this study, we investigated the effect of an  $\text{Fe}_3\text{O}_4@\text{SiO}_2/\text{Co-Cr-B}$  magnetic catalyst on sodium borohydride ( $\text{NaBH}_4$ ) hydrolysis for hydrogen generation. The catalyst was synthesized by a hydrothermal method, and various parameters, such as  $\text{NaOH}\%$ ,  $\text{NaBH}_4\%$ , catalyst amount, and temperature, were systematically examined. At room temperature, the activation energy according to Langmuir–Hinshelwood and the  $n$ th-order kinetic models was determined to be  $23.60 \text{ kJ mol}^{-1}$  and  $20.75 \text{ kJ mol}^{-1}$  respectively, while the hydrogen generation rate under optimal conditions was measured to be  $22.20 \text{ L g}_{\text{metal}}^{-1} \text{ min}^{-1}$ . Nanoparticle characterization revealed a uniform size distribution in the range of 100–200 nm, with spherical morphology and well-dispersed particles, indicating the successful synthesis of the catalyst.

The magnetic recovery feature of the  $\text{Fe}_3\text{O}_4@\text{SiO}_2/\text{Co-Cr-B}$  catalyst simplifies the separation process, reduces the downtime, and enables continuous operation, making it highly practical for industrial applications. Additionally, the use of non-noble metals, such as Co and Cr, offers a cost-effective

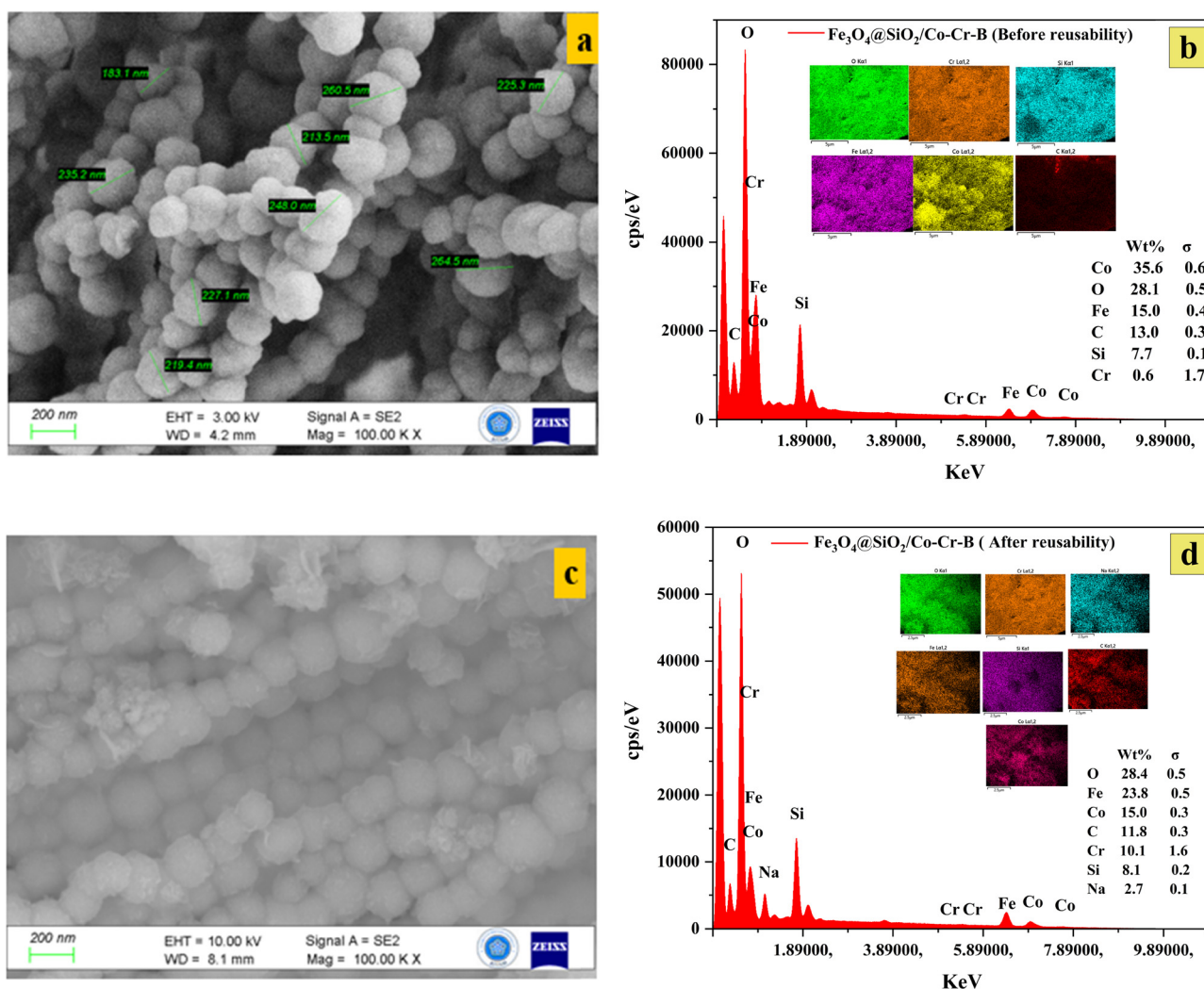


Fig. 15 FESEM/EDX image of the synthesized  $\text{Fe}_3\text{O}_4@\text{SiO}_2/\text{Co-Cr-B}$  catalyst (a) and (b) before the reusability test and (c) and (d) after the reusability test.

alternative to precious metal catalysts, enhancing the feasibility of large-scale production. Future work should explore the integration of this catalyst into continuous-flow reactors, which are widely employed in the chemical industry, to further optimize its application. Combining a catalyst with renewable hydrogen sources could also strengthen its role in achieving global sustainability goals, such as those outlined in the Paris Agreement.

## Author contributions

Houssem Lakhali: writing – original draft, validation, methodology, investigation. Ömer Şahin: writing – review & editing, visualization, validation, supervision, resources, methodology, formal analysis, conceptualization. Ayhan Abdullah Ceyhan: writing – original draft, visualization, validation, supervision, resources, project administration, methodology, investigation, funding acquisition, formal analysis, conceptualization.

## Data availability

The data can be obtained on reasonable request from the corresponding author.

## Conflicts of interest

The authors declare that they have no known competing financial interests or personal relationships that could have appeared to influence the work reported in this paper.

## Acknowledgements

This study was supported by Konya Technical University's Scientific Research Projects (BAP) Coordination Unit (Project No. 221116033).

## References

- 1 A. Azam, M. Rafiq, M. Shafique and J. Yuan, Towards achieving environmental sustainability: the role of nuclear energy, renewable energy, and ICT in the top-five carbon emitting countries, *Front. Energy Res.*, 2022, 9, DOI: [10.3389/fenrg.2021.804706](https://doi.org/10.3389/fenrg.2021.804706).
- 2 R. Saidur, E. A. Abdelaziz, A. Demirbas, M. S. Hossain and S. Mekhilef, A review on biomass as a fuel for boilers, *Renewable Sustainable Energy Rev.*, 2011, 15, 2262–2289, DOI: [10.1016/j.rser.2011.02.015](https://doi.org/10.1016/j.rser.2011.02.015).
- 3 F. Perera, Pollution from fossil-fuel combustion is the leading environmental threat to global pediatric health and equity: Solutions exist, *Int. J. Environ. Res. Public Health*, 2018, 15, 16, DOI: [10.3390/ijerph15010016](https://doi.org/10.3390/ijerph15010016).
- 4 Q. Ding, J. Huang, J. Chen and X. Luo, Climate warming, renewable energy consumption and rare earth market: Evidence from the United States, *Energy*, 2024, 130276, DOI: [10.1016/j.energy.2024.130276](https://doi.org/10.1016/j.energy.2024.130276).
- 5 Q. Wang, Z. Sun, J. Guo and R. Li, The more effective option to combat environmental degradation: Energy efficiency vs. renewable energy vs. natural gas?, *Energy*, 2023, 283, 128512, DOI: [10.1038/s41586-021-03821-8](https://doi.org/10.1038/s41586-021-03821-8).
- 6 X. Shen, Q. Wang, Q. Wu, S. Guo, Z. Zhang and Z. Sun, *et al.*, CoB supported on Ag-activated TiO<sub>2</sub> as a highly active catalyst for hydrolysis of alkaline NaBH<sub>4</sub> solution, *Energy*, 2015, 90, 464–474, DOI: [10.1016/j.energy.2015.07.075](https://doi.org/10.1016/j.energy.2015.07.075).
- 7 A. M. M. I. Qureshy and I. Dincer, Energy and exergy analyses of an integrated renewable energy system for hydrogen production, *Energy*, 2020, 204, 117945, DOI: [10.1016/j.energy.2020.117945](https://doi.org/10.1016/j.energy.2020.117945).
- 8 Z. Sun, J. Hong, T. Zhang, B. Sun, B. Yang and L. Lu, *et al.*, Hydrogen engine operation strategies: recent progress, industrialization challenges, and perspectives, *Int. J. Hydrogen Energy*, 2023, 48, 366–392, DOI: [10.1016/j.ijhydene.2022.09.256](https://doi.org/10.1016/j.ijhydene.2022.09.256).
- 9 L. Luo, L. Chen, L. Li, S. Liu, Y. Li and C. Li, *et al.*, High-entropy alloys for solid hydrogen storage: a review, *Int. J. Hydrogen Energy*, 2023, 50, 406–430, DOI: [10.1016/j.ijhydene.2023.07.146](https://doi.org/10.1016/j.ijhydene.2023.07.146).
- 10 P. Muthukumar, A. Kumar, M. Afzal, S. Bhogilla, P. Sharma and A. Parida, *et al.*, Review on large-scale hydrogen storage systems for better sustainability, *Int. J. Hydrogen Energy*, 2023, 48, 33223, DOI: [10.1016/j.ijhydene.2023.04.304](https://doi.org/10.1016/j.ijhydene.2023.04.304).
- 11 D. Xu, X. Lai, W. Guo, X. Zhang, C. Wang and P. Dai, Efficient catalytic properties of SO<sub>4</sub><sup>2-</sup>/M<sub>x</sub>O<sub>y</sub> (M = Cu, Co, Fe) catalysts for hydrogen generation by methanolysis of sodium borohydride, *Int. J. Hydrogen Energy*, 2018, 43, 6594–6602, DOI: [10.1016/j.ijhydene.2018.02.074](https://doi.org/10.1016/j.ijhydene.2018.02.074).
- 12 M. Kaya, Evaluating organic waste sources (spent coffee ground) as metal-free catalyst for hydrogen generation by the methanolysis of sodium borohydride, *Int. J. Hydrogen Energy*, 2020, 45, 12743–12754, DOI: [10.1016/j.ijhydene.2019.10.180](https://doi.org/10.1016/j.ijhydene.2019.10.180).
- 13 G. Bozkurt, A. Özer and A. B. Yurtcan, Development of effective catalysts for hydrogen generation from sodium borohydride: Ru, Pt, Pd nanoparticles supported on Co<sub>3</sub>O<sub>4</sub>, *Energy*, 2019, 180, 702–713, DOI: [10.1016/j.energy.2019.04.196](https://doi.org/10.1016/j.energy.2019.04.196).
- 14 F. Xu, J. Ren, J. Ma, Y. Wang, K. Zhang and Z. Cao, *et al.*, A review of hydrogen production kinetics from the hydrolysis of NaBH<sub>4</sub> solution catalyzed by Co-based catalysts, *Int. J. Hydrogen Energy*, 2023, 50, 827–844, DOI: [10.1016/j.ijhydene.2023.08.142](https://doi.org/10.1016/j.ijhydene.2023.08.142).
- 15 M. Munir, M. Ahmad, M. Saeed, A. Waseem, A.-S. Nizami and S. Sultana, *et al.*, Biodiesel production from novel non-edible caper (*Capparis spinosa* L.) seeds oil employing Cu–Ni doped ZrO<sub>2</sub> catalyst, *Renewable Sustainable Energy Rev.*, 2021, 138, 110558, DOI: [10.1016/j.rser.2020.110558](https://doi.org/10.1016/j.rser.2020.110558).
- 16 J. A. Calles, A. Carrero, A. J. Vizcaíno and P. J. Megía, Agglomerated Co–Cr/SBA-15 catalysts for hydrogen production through acetic acid steam reforming, *Int. J. Hydrogen Energy*, 2020, 45, 15941–15950, DOI: [10.1016/j.ijhydene.2019.05.237](https://doi.org/10.1016/j.ijhydene.2019.05.237).
- 17 R. Li, F. Zhang, J. Zhang and H. Dong, Catalytic hydrolysis of NaBH<sub>4</sub> over titanate nanotube supported Co for hydrogen production, *Int. J. Hydrogen Energy*, 2022, 47, 5260–5268, DOI: [10.1016/j.ijhydene.2021.11.143](https://doi.org/10.1016/j.ijhydene.2021.11.143).





- 18 F. Mirshafiee and M. Rezaei, Co/Fe<sub>3</sub>O<sub>4</sub>@GO catalyst for one-step hydrogen generation from hydrolysis of NaBH<sub>4</sub>: Optimization and kinetic study, *Int. J. Hydrogen Energy*, 2023, **48**, 32356–32370, DOI: [10.1016/j.ijhydene.2023.04.337](https://doi.org/10.1016/j.ijhydene.2023.04.337).
- 19 Q. Sun, X.-Q. Zhang, Y. Wang and A.-H. Lu, Recent progress on core-shell nanocatalysts, *Chin. J. Catal.*, 2015, **36**, 683–691, DOI: [10.1016/S1872-2067\(14\)60298-9](https://doi.org/10.1016/S1872-2067(14)60298-9).
- 20 F. Ke, J. Yuan, C. Zhang, S. Ye, K. Ramachandraiah and H. Pang, Core-shell nanostructured metal-organic frameworks with encapsulated magnetic nanoparticles for magnetically recyclable catalysis, *Coord. Chem. Rev.*, 2024, **518**, 216116, DOI: [10.1016/j.ccr.2024.216116](https://doi.org/10.1016/j.ccr.2024.216116).
- 21 M. S. Ece, S. Kutluay, O. Şahin and S. Horoz, Development of novel Fe<sub>3</sub>O<sub>4</sub>/AC@ SiO<sub>2</sub>@1,4-DAAQ magnetic nanoparticles with outstanding VOC removal capacity: characterization, optimization, reusability, kinetics, and equilibrium studies, *Ind. Eng. Chem. Res.*, 2020, **59**, 21106–21123, DOI: [10.1021/acs.iecr.0c03883](https://doi.org/10.1021/acs.iecr.0c03883).
- 22 A. Khalid, R. M. Ahmed, M. Taha and T. S. Soliman, Fe<sub>3</sub>O<sub>4</sub> nanoparticles and Fe<sub>3</sub>O<sub>4</sub>@SiO<sub>2</sub> core-shell: synthesis, structural, morphological, linear, and nonlinear optical properties, *J. Alloys Compd.*, 2023, **947**, 169639, DOI: [10.1016/j.jallcom.2023.169639](https://doi.org/10.1016/j.jallcom.2023.169639).
- 23 L. Wang, J.-X. Guo, X.-W. Chen, C. Li, W. Kiyangi and R.-Y. Xiong, *et al.*, Fe<sub>3</sub>O<sub>4</sub>/AM-PAA/Ni nanomagnetic spheres: A breakthrough in in-situ catalytic reduction of heavy oil viscosity, *J. Anal. Appl. Pyrolysis*, 2024, **181**, 106664, DOI: [10.1016/j.jaap.2024.106664](https://doi.org/10.1016/j.jaap.2024.106664).
- 24 Z. Zhu, Z. Lu, D. Wang, X. Tang, Y. Yan and W. Shi, *et al.*, Construction of high-dispersed Ag/Fe<sub>3</sub>O<sub>4</sub>/g-C<sub>3</sub>N<sub>4</sub> photocatalyst by selective photo-deposition and improved photocatalytic activity, *Appl. Catal., B*, 2016, **182**, 115–122, DOI: [10.1016/j.apcatb.2015.09.029](https://doi.org/10.1016/j.apcatb.2015.09.029).
- 25 A. F. Baye, M. W. Abebe, R. Appiah-Ntiamoah and H. Kim, Engineered iron-carbon-cobalt (Fe<sub>3</sub>O<sub>4</sub>@ C-Co) core-shell composite with synergistic catalytic properties towards hydrogen generation via NaBH<sub>4</sub> hydrolysis, *J. Colloid Interface Sci.*, 2019, **543**, 273–284, DOI: [10.1016/j.jcis.2019.02.065](https://doi.org/10.1016/j.jcis.2019.02.065).
- 26 Z. Li, H. Li, L. Wang, T. Liu, T. Zhang and G. Wang, *et al.*, Hydrogen generation from catalytic hydrolysis of sodium borohydride solution using supported amorphous alloy catalysts (Ni-Co-P/γ-Al<sub>2</sub>O<sub>3</sub>), *Int. J. Hydrogen Energy*, 2014, **39**, 14935–14941, DOI: [10.1016/j.ijhydene.2014.07.063](https://doi.org/10.1016/j.ijhydene.2014.07.063).
- 27 D. Kılınc and Ö. Şahin, Effective TiO<sub>2</sub> supported Cu-Complex catalyst in NaBH<sub>4</sub> hydrolysis reaction to hydrogen generation, *Int. J. Hydrogen Energy*, 2019, **44**, 18858–18865, DOI: [10.1016/j.ijhydene.2018.12.225](https://doi.org/10.1016/j.ijhydene.2018.12.225).
- 28 M. S. İzgi, O. Baytar, Ö. Şahin and H. Ç. Kazıcı, CeO<sub>2</sub> supported multimetallic nano materials as an efficient catalyst for hydrogen generation from the hydrolysis of NaBH<sub>4</sub>, *Int. J. Hydrogen Energy*, 2020, **45**, 34857–34866, DOI: [10.1016/j.ijhydene.2020.04.034](https://doi.org/10.1016/j.ijhydene.2020.04.034).
- 29 W. Chen, J. Ji, X. Duan, G. Qian, P. Li and X. Zhou, *et al.*, Unique reactivity in Pt/CNT catalyzed hydrolytic dehydrogenation of ammonia borane, *Chem. Commun.*, 2014, **50**, 2142–2144, DOI: [10.1039/C3CC48027E](https://doi.org/10.1039/C3CC48027E).
- 30 N. Erat, G. Bozkurt and A. Özer, Co/CuO–NiO–Al<sub>2</sub>O<sub>3</sub> catalyst for hydrogen generation from hydrolysis of NaBH<sub>4</sub>, *Int. J. Hydrogen Energy*, 2022, **47**, 24255–24267, DOI: [10.1016/j.ijhydene.2022.05.178](https://doi.org/10.1016/j.ijhydene.2022.05.178).
- 31 S. Dou, W. Zhang, Y. Yang, S. Zhou, X. Rao and P. Yan, *et al.*, Shaggy-like Ru-clusters decorated core-shell metal-organic framework-derived CoOx@NPC as high-efficiency catalyst for NaBH<sub>4</sub> hydrolysis, *Int. J. Hydrogen Energy*, 2021, **46**, 7772–7781, DOI: [10.1016/j.ijhydene.2020.12.011](https://doi.org/10.1016/j.ijhydene.2020.12.011).
- 32 Y. Chi, Q. Yuan, Y. Li, J. Tu, L. Zhao and N. Li, *et al.*, Synthesis of Fe<sub>3</sub>O<sub>4</sub>@ SiO<sub>2</sub>–Ag magnetic nanocomposite based on small-sized and highly dispersed silver nanoparticles for catalytic reduction of 4-nitrophenol, *J. Colloid Interface Sci.*, 2012, **383**, 96–102, DOI: [10.1016/j.jcis.2012.06.027](https://doi.org/10.1016/j.jcis.2012.06.027).
- 33 T. Yu, X. Zhao, L. Ma and X. Shen, Intercalation and electrochemical behaviors of layered FeOCl cathode material in chloride ion battery, *Mater. Res. Bull.*, 2017, **96**, 485–490, DOI: [10.1016/j.materresbull.2017.03.070](https://doi.org/10.1016/j.materresbull.2017.03.070).
- 34 A. Saini, S. K. Jat, D. S. Shekhawat, A. Kumar, V. Dhayal and D. C. Agarwal, Oxime-modified aluminium (III) alkoxides: potential precursors for γ-alumina nano-powders and optically transparent alumina film, *Mater. Res. Bull.*, 2017, **93**, 373–380, DOI: [10.1016/j.materresbull.2017.04.011](https://doi.org/10.1016/j.materresbull.2017.04.011).
- 35 Y. Wei, B. Han, X. Hu, Y. Lin, X. Wang and X. Deng, Synthesis of Fe<sub>3</sub>O<sub>4</sub> nanoparticles and their magnetic properties, *Procedia Eng.*, 2012, **27**, 632–637, DOI: [10.1016/j.proeng.2011.12.498](https://doi.org/10.1016/j.proeng.2011.12.498).
- 36 M. Ş. Ece, A. Ekinçi, S. Kutluay, Ö. Şahin and S. Horoz, Facile synthesis and comprehensive characterization of Ni-decorated amine groups-immobilized Fe<sub>3</sub>O<sub>4</sub>@SiO<sub>2</sub> magnetic nanoparticles having enhanced solar cell efficiency, *J. Mater. Sci.: Mater. Electron.*, 2021, **32**, 18192–18204, DOI: [10.1007/s10854-021-06361-z](https://doi.org/10.1007/s10854-021-06361-z).
- 37 J. Mohammed, K. M. Batoo, G. Mukhtar, J. P. Labis, E. H. Raslan and M. Hadi, *et al.*, Crystal-structure analysis, Raman spectroscopy, dielectric measurements, magnetic and optical properties of Cr<sup>3+</sup>–Ni<sup>2+</sup>-substituted Co<sub>2</sub>Y-type barium hexaferrites, *Mater. Res. Bull.*, 2022, **145**, 111564, DOI: [10.1016/j.materresbull.2021.111564](https://doi.org/10.1016/j.materresbull.2021.111564).
- 38 Q. Zhang, J. Jiang, F. Gao, G. Zhang, X. Zhan and F. Chen, Engineering high-effective antifouling polyether sulfone membrane with P (PEG-PDMS-KH570)@SiO<sub>2</sub> nanocomposite via in-situ sol-gel process, *Chem. Eng. J.*, 2017, **321**, 412–423, DOI: [10.1016/j.cej.2017.03.105](https://doi.org/10.1016/j.cej.2017.03.105).
- 39 G. Gu, T. Ma, F. Chen, C. Han, H. Li and F. Xu, Controlling electromagnetic and mechanical behaviors of geopolymer matrix with nano-SiO<sub>2</sub>@Fe<sub>3</sub>O<sub>4</sub> magnetofluid for soft magnetic applications, *Cem. Concr. Compos.*, 2023, 105370, DOI: [10.1016/j.cemconcomp.2023.105370](https://doi.org/10.1016/j.cemconcomp.2023.105370).
- 40 M. A. Mustafa, Q. A. Qasim, A. B. Mahdi, S. E. Izzat, Y. S. Alnassar and E. S. Abood, *et al.*, Supercapacitor performance of Fe<sub>3</sub>O<sub>4</sub> and Fe<sub>3</sub>O<sub>4</sub>@SiO<sub>2</sub>-bis (aminopyridine)-Cu hybrid nanocomposite, *Int. J. Electrochem. Sci.*, 2022, **17**, 221057, DOI: [10.20964/2022.10.49](https://doi.org/10.20964/2022.10.49).
- 41 X. Su, C. Chan, J. Shi, M.-K. Tsang, Y. Pan and C. Cheng, *et al.*, A graphene quantum dot@Fe<sub>3</sub>O<sub>4</sub>@SiO<sub>2</sub> based



- nanoprobe for drug delivery sensing and dual-modal fluorescence and MRI imaging in cancer cells, *Biosens. Bioelectron.*, 2017, **92**, 489–495, DOI: [10.1016/j.bios.2016.10.076](#).
- 42 Y. Chen and J. Nan, A strategy to alleviate membrane fouling by optimizing the structure of the cake layer formed by flocs deposited directly on the membrane in the ultrafiltration process through coagulation and nanoscale  $\text{Fe}_3\text{O}_4/\text{Fe}_3\text{O}_4@\text{SiO}_2$  load, *J. Membr. Sci.*, 2023, **680**, 121729, DOI: [10.1016/j.memsci.2023.121729](#).
  - 43 M. Sadeghi, Z. Moghimifar and H. Javadian,  $\text{Fe}_3\text{O}_4@\text{SiO}_2$  nanocomposite immobilized with cellulase enzyme: Stability determination and biological activity, *Chem. Phys. Lett.*, 2023, **811**, 140161, DOI: [10.1016/j.cplett.2022.140161](#).
  - 44 V. K. Yadav, D. Ali, S. H. Khan, G. Gnanamoorthy, N. Choudhary and K. K. Yadav, *et al.*, Synthesis and characterization of amorphous iron oxide nanoparticles by the sonochemical method and their application for the remediation of heavy metals from wastewater, *Nanomaterials*, 2020, **10**, 1551, DOI: [10.3390/nano10081551](#).
  - 45 A. G. Jacob, R. A. Wahab and M. Misson, Operational stability, regenerability, and thermodynamics studies on biogenic silica/magnetite/graphene oxide nanocomposite-activated *Candida rugosa* Lipase, *Polymers*, 2021, 13–3854, DOI: [10.3390/polym13213854](#).
  - 46 K. Al-Mokhalelati, F. Karabet, A. W. Allaf, M. Naddaf and A. G. Al Lafi, Spectroscopic investigations to reveal synergy between polystyrene waste and paraffin wax in superhydrophobic sand, *Sci. Rep.*, 2023, **13**, 9810, DOI: [10.1038/s41598-023-36987-4](#).
  - 47 S. Kutluay, Ö. Şahin and M. Ş. Ece, Fabrication and characterization of  $\text{Fe}_3\text{O}_4/\text{perlite}$ ,  $\text{Fe}_3\text{O}_4/\text{perlite}@\text{SiO}_2$ , and  $\text{Fe}_3\text{O}_4/\text{perlite}@\text{SiO}_2@\text{sulfanilamide}$  magnetic nanomaterials, *Appl. Phys. A: Mater. Sci. Process.*, 2022, **128**, 222, DOI: [10.1007/s00339-022-05369-4](#).
  - 48 V. Vats, G. Melton, M. Islam and V. V. Krishnan, FTIR spectroscopy as a convenient tool for detection and identification of airborne Cr (VI) compounds arising from arc welding fumes, *J. Hazard. Mater.*, 2023, **448**, 130862, DOI: [10.1016/j.jhazmat.2023.130862](#).
  - 49 R. Huang, X. Ma, X. Li, L. Guo, X. Xie and M. Zhang, *et al.*, A novel ion-imprinted polymer based on graphene oxide-mesoporous silica nanosheet for fast and efficient removal of chromium (VI) from aqueous solution, *J. Colloid Interface Sci.*, 2018, **514**, 544–553, DOI: [10.1016/j.jcis.2017.12.065](#).
  - 50 A. A. Elfadl, A. H. Bashal, T. H. Habeeb, M. A. H. Khalafalla, N. S. Alkayal and K. D. Khalil, Preparation, Characterization, Dielectric Properties, and AC Conductivity of Chitosan Stabilized Metallic Oxides CoO and SrO: Experiments and Tight Binding Calculations, *Polymers*, 2023, 15–4132, DOI: [10.3390/polym15204132](#).
  - 51 O. A. Fouad, S. A. Makhlof, G. A. M. Ali and A. Y. El-Sayed, Cobalt/silica nanocomposite via thermal calcination-reduction of gel precursors, *Mater. Chem. Phys.*, 2011, **128**, 70–76, DOI: [10.1016/j.matchemphys.2011.02.072](#).
  - 52 M. S. Izgi, M. Ş. Ece, H. Ç. Kazici, Ö. Şahin and E. Onat, Hydrogen production by using Ru nanoparticle decorated with  $\text{Fe}_3\text{O}_4@\text{SiO}_2-\text{NH}_2$  core-shell microspheres, *Int. J. Hydrogen Energy*, 2020, **45**, 30415–30430, DOI: [10.1016/j.ijhydene.2020.08.043](#).
  - 53 J. Wu, K. Ke, N. Qin, E. Lin, Z. Kang and D. Bao, Magnetically retrievable  $\text{Fe}_3\text{O}_4@\text{SiO}_2@\text{ZnO}$  piezo-photocatalyst: Synthesis and multiple catalytic properties, *J. Colloid Interface Sci.*, 2023, **636**, 167–175, DOI: [10.1016/j.jcis.2023.01.009](#).
  - 54 Ö. Şahin, A. A. Ceyhan and H. Lakhali, Core-shell doping of cerium oxide with (Cr-Fe/Co)-B catalyst for enhanced hydrogen evolution in borohydride hydrolysis systems: performance and catalytic efficiency, *Res. Chem. Intermed.*, 2025, 1–34, DOI: [10.1007/s11164-025-05571-y](#).
  - 55 M. Khoshnam and H. Salimijazi, Synthesis and characterization of magnetic-photocatalytic  $\text{Fe}_3\text{O}_4/\text{SiO}_2/\alpha\text{-Fe}_2\text{O}_3$  nano core-shell, *Surf. Interfaces*, 2021, **26**, 101322, DOI: [10.1016/j.surfin.2021.101322](#).
  - 56 C. Hui, C. Shen, J. Tian, L. Bao, H. Ding and C. Li, *et al.*, Core-shell  $\text{Fe}_3\text{O}_4@\text{SiO}_2$  nanoparticles synthesized with well-dispersed hydrophilic  $\text{Fe}_3\text{O}_4$  seeds, *Nanoscale*, 2011, **3**(2), 701–705, DOI: [10.1039/c0nr00497a](#).
  - 57 L. Guo, K. Zhang, H. Shen, C. Wang, Q. Zhao and D. Wang, *et al.*, Magnetically recyclable  $\text{Fe}_3\text{O}_4@\text{SiO}_2/\text{Bi}_2\text{WO}_6-x\text{F}_{2x}$  photocatalyst with well-designed core-shell nanostructure for the reduction of Cr(VI), *Chem. Eng. J.*, 2019, **370**, 1552–1533, DOI: [10.1016/j.cej.2019.04.037](#).
  - 58 L. Sun, Z. Chen, X. Meng, S. Sun, Z. Lv and Q. Liang, *et al.*, Construction of  $\text{Fe}_3\text{O}_4/x\text{SiO}_2/y\text{SiO}_2$  Nanoparticles for Pesticide Removal from Water: Improved Dispersion Stability and Adsorption Capacity, *Langmuir*, 2023, **39**, 8749–8759, DOI: [10.1021/acs.langmuir.3c00736](#).
  - 59 F. Zarei, F. B. Jahromi, A. Elhambakhsh and P. Keshavarz, Enhanced  $\text{CO}_2$  absorption and reduced regeneration energy consumption using modified magnetic NPs, *Energy*, 2023, **278**, 127776, DOI: [10.1016/j.energy.2023.127776](#).
  - 60 Z. Jia, J. Zhang, F. Lv, Y. Hou, J. Liu and S. Yu, *et al.*, Synthesis of  $\text{Fe}_3\text{O}_4@\text{SiO}_2@\text{C}/\text{Ni}$  microspheres for enhanced electromagnetic wave absorption, *J. Non Cryst. Solids*, 2023, **622**, 122659, DOI: [10.1016/j.jnoncrysol.2023.122659](#).
  - 61 M. Nasrollahzadeh, Z. Issaabadi and R. Safari, Synthesis, characterization and application of  $\text{Fe}_3\text{O}_4@\text{SiO}_2$  nanoparticles supported palladium(II) complex as a magnetically catalyst for the reduction of 2,4-dinitrophenylhydrazine, 4-nitrophenol and chromium(VI): A combined theoretical (DFT) and experimental study, *Sep. Purif. Technol.*, 2019, **209**, 136–144, DOI: [10.1016/j.seppur.2018.07.022](#).
  - 62 M. M. Sabzehmeidani, H. Karimi and M. Ghaedi, Nanofibers based quaternary  $\text{CeO}_2/\text{Co}_3\text{O}_4/\text{Ag}/\text{Ag}_3\text{PO}_4$  S-scheme heterojunction photocatalyst with enhanced degradation of organic dyes, *Mater. Res. Bull.*, 2022, **147**, 111629, DOI: [10.1016/j.materresbull.2021.111629](#).
  - 63 R. Fernandes, N. Patel and A. Miotello, Hydrogen generation by hydrolysis of alkaline  $\text{NaBH}_4$  solution with Cr-promoted Co-B amorphous catalyst, *Appl. Catal., B*, 2009, **92**, 68–74, DOI: [10.1016/j.apcatb.2009.07.019](#).
  - 64 Z. Kanwal, M. A. Raza, F. Manzoor, S. Riaz, G. Jabeen and S. Fatima, *et al.*, A comparative assessment of nanotoxicity



- induced by metal (silver, nickel) and metal oxide (cobalt, chromium) nanoparticles in *Labeo rohita*, *Nanomaterials*, 2019, **9**, 309, DOI: [10.3390/nano9020309](https://doi.org/10.3390/nano9020309).
- 65 C.-C. Yang, M.-S. Chen and Y.-W. Chen, Hydrogen generation by hydrolysis of sodium borohydride on CoB/SiO<sub>2</sub> catalyst, *Int. J. Hydrogen Energy*, 2011, **36**, 1418–1423, DOI: [10.1016/j.ijhydene.2010.11.006](https://doi.org/10.1016/j.ijhydene.2010.11.006).
- 66 S. Zhao, J. Zhang, Z. Chen, Y. Tong, J. Shen and D. Li, *et al.*, Hydrogen generation and simultaneous removal of Cr (VI) by hydrolysis of NaBH<sub>4</sub> using Fe-Al-Si composite as accelerator, *Chemosphere*, 2019, **223**, 131–139, DOI: [10.1016/j.chemosphere.2019.02.050](https://doi.org/10.1016/j.chemosphere.2019.02.050).
- 67 S. S. Alterary and A. AlKhamees, Synthesis, surface modification, and characterization of Fe<sub>3</sub>O<sub>4</sub>@SiO<sub>2</sub> core@ shell nanostructure, *Green Process Synth.*, 2021, **10**, 384–391, DOI: [10.1515/gps-2021-0031](https://doi.org/10.1515/gps-2021-0031).
- 68 D. Channei, B. Inceesungvorn, N. Wetchakun and S. Phanichphant, Synthesis of Fe<sub>3</sub>O<sub>4</sub>/SiO<sub>2</sub>/CeO<sub>2</sub> core-shell magnetic and their application as photocatalyst, *J. Nanosci. Nanotechnol.*, 2014, **14**, 7756–7762, DOI: [10.1166/jnn.2014.9427](https://doi.org/10.1166/jnn.2014.9427).
- 69 M. H. Youn, J. G. Seo and I. K. Song, Hydrogen production by auto-thermal reforming of ethanol over nickel catalyst supported on metal oxide-stabilized zirconia, *Int. J. Hydrogen Energy*, 2010, **35**, 3490–3498, DOI: [10.1016/j.ijhydene.2010.01.121](https://doi.org/10.1016/j.ijhydene.2010.01.121).
- 70 V. G. Deshmane, R. Y. Abrokwhah and D. Kuila, Mesoporous nanocrystalline TiO<sub>2</sub> supported metal (Cu, Co, Ni, Pd, Zn, and Sn) catalysts: Effect of metal-support interactions on steam reforming of methanol, *J. Mol. Catal. A: Chem.*, 2015, **408**, 202–213, DOI: [10.1016/j.molcata.2015.07.023](https://doi.org/10.1016/j.molcata.2015.07.023).
- 71 M. Labaki, S. Siffert, J.-F. Lamonier, E. A. Zhilinskaya and A. Aboukais, Total oxidation of propene and toluene in the presence of zirconia doped by copper and yttrium: role of anionic vacancies, *Appl. Catal., B*, 2003, **43**, 261–271, DOI: [10.1016/S0926-3373\(02\)00312-0](https://doi.org/10.1016/S0926-3373(02)00312-0).
- 72 R. Yang, Y. Fan and R. Zhu, One step preparation of in-situ carbon-modified artificial leaf BiVO<sub>4</sub> for photocatalytic pollutants degradation, *Mater. Res. Bull.*, 2020, **124**, 110756, DOI: [10.1016/j.materresbull.2019.110756](https://doi.org/10.1016/j.materresbull.2019.110756).
- 73 G. Bancroft, H. Nesbitt, R. Ho, D. Shaw, J. Tse and M. Biesinger, Toward a comprehensive understanding of solid-state core-level XPS linewidths: Experimental and theoretical studies on the Si 2p and O 1s linewidths in silicates, *Phys. Rev. B: Condens. Matter Mater. Phys.*, 2009, **80**, 75405, DOI: [10.1103/physrevb.80.075405](https://doi.org/10.1103/physrevb.80.075405).
- 74 H. Tian, L. Hu, C. Zhang, S. Chen, J. Sheng and L. Mo, *et al.*, Enhanced photovoltaic performance of dye-sensitized solar cells using a highly crystallized mesoporous TiO<sub>2</sub> electrode modified by boron doping, *J. Mater. Chem.*, 2011, **21**, 863–868, DOI: [10.1039/C0JM02941F](https://doi.org/10.1039/C0JM02941F).
- 75 T. Khai, H. Na, D. Kwak, Y. Kwon, H. Ham and K. Shim, *et al.*, Comparison study of structural and optical properties of boron-doped and undoped graphene oxide films, *Chem. Eng. J.*, 2012, **211**, 369–377, DOI: [10.1016/j.cej.2012.09.081](https://doi.org/10.1016/j.cej.2012.09.081).
- 76 G. Yang, G. Möbus and R. J. Hand, Cerium and boron chemistry in doped borosilicate glasses examined by EELS, *Micron*, 2006, **37**, 433–441, DOI: [10.1039/d2qi00838f](https://doi.org/10.1039/d2qi00838f).
- 77 W. Jiao, Q. Su, J. Ge, S. Dong, D. Wang and M. Zhang, *et al.*, Mo<sub>2</sub>C quantum dots decorated ultrathin carbon nanosheets self-assembled into nanoflowers toward highly catalytic cathodes for Li-O<sub>2</sub> batteries, *Mater. Res. Bull.*, 2021, **133**, 111020, DOI: [10.1016/j.materresbull.2020.111020](https://doi.org/10.1016/j.materresbull.2020.111020).
- 78 W. Phae-ngam, J. Prathumsit, T. Chaikereee, N. Bodinithitkul, T. Lertvanithphol and H. Nakajima, *et al.*, Characterization of ternary ZrHfN thin films deposited by closed-field dual-cathode DC unbalanced reactive magnetron sputtering: A preliminary investigation on their reusable SERS with high thermal stability, *Mater. Res. Bull.*, 2025, 113301, DOI: [10.1016/j.materresbull.2025.113301](https://doi.org/10.1016/j.materresbull.2025.113301).
- 79 V. Singh, S. N. Sarangi, D. Samal and R. Nath, Magnetic phase transition and magneto-elastic coupling in Fe<sub>1+x</sub>Cr<sub>2-x</sub>Se<sub>4</sub> (x = 0.0–0.50), *Mater. Res. Bull.*, 2022, **155**, 111941, DOI: [10.1016/j.materresbull.2022.111941](https://doi.org/10.1016/j.materresbull.2022.111941).
- 80 X. Duan, X. Wang, F. Yu and X. Liu, Effects of Co content and annealing temperature on the structure and optical properties of Co<sub>x</sub>Mg<sub>1-x</sub>Al<sub>2</sub>O<sub>4</sub> nanoparticles, *Mater. Chem. Phys.*, 2012, **137**, 652–659, DOI: [10.1016/j.matchemphys.2012.10.016](https://doi.org/10.1016/j.matchemphys.2012.10.016).
- 81 V. Sahoo, R. N. Bhowmik and S. A. Khan, Enhancement of electrical conductivity, optical band gap and ferromagnetic properties by co-doping of Co and Ti ions in canted anti-ferromagnetic hematite (α-Fe<sub>2</sub>O<sub>3</sub>) system, *Mater. Chem. Phys.*, 2023, **296**, 127298, DOI: [10.1016/j.matchemphys.2023.127298](https://doi.org/10.1016/j.matchemphys.2023.127298).
- 82 N. Patel, R. Fernandes and A. Miotello, Promoting effect of transition metal-doped Co-B alloy catalysts for hydrogen production by hydrolysis of alkaline NaBH<sub>4</sub> solution, *J. Catal.*, 2010, **271**, 315–324, DOI: [10.1016/j.jcat.2010.02.014](https://doi.org/10.1016/j.jcat.2010.02.014).
- 83 M. Makiabadi, T. Shamspur and A. Mostafavi, Performance improvement of oxygen on the carbon substrate surface for dispersion of cobalt nanoparticles and its effect on hydrogen generation rate via NaBH<sub>4</sub> hydrolysis, *Int. J. Hydrogen Energy*, 2020, **45**, 1706–1718, DOI: [10.1016/j.ijhydene.2019.11.026](https://doi.org/10.1016/j.ijhydene.2019.11.026).
- 84 E. Fangaj, A. A. Ali, F. Güngör, S. Bektaş and A. A. Ceyhan, The use of metallurgical waste sludge as a catalyst in hydrogen production from sodium borohydride, *Int. J. Hydrogen Energy*, 2020, **45**, 13322–13329, DOI: [10.1016/j.ijhydene.2020.03.043](https://doi.org/10.1016/j.ijhydene.2020.03.043).
- 85 M. Altınsoy and A. A. Ceyhan, Synthesis of cobalt-doped catalyst for NaBH<sub>4</sub> hydrolysis using eggshell biowaste, *Int. J. Hydrogen Energy*, 2023, **48**, 28018–28033, DOI: [10.1016/j.ijhydene.2023.04.047](https://doi.org/10.1016/j.ijhydene.2023.04.047).
- 86 Y.-H. Huang, C.-C. Su, S.-L. Wang and M.-C. Lu, Development of Al<sub>2</sub>O<sub>3</sub> carrier-Ru composite catalyst for hydrogen generation from alkaline NaBH<sub>4</sub> hydrolysis, *Energy*, 2012, **46**, 242–247, DOI: [10.1016/j.energy.2012.08.027](https://doi.org/10.1016/j.energy.2012.08.027).
- 87 X. Feng, Z. Song, T. Guo, R. Yang, Y. Liu and X. Chen, *et al.*, Insights into the effect of surface functional groups on catalytic performance for hydrogen generation from sodium borohydride, *RSC Adv.*, 2016, **6**, 113260, DOI: [10.1039/c6ra25016e](https://doi.org/10.1039/c6ra25016e).
- 88 C. Kaya, J. H. Özdemir, H. Elçiçek, O. K. Özdemir, G. Kökkülünk and K. Ünlügençoğlu, Enhancing the efficiency of sodium borohydride hydrolysis with a novel CoB-Triton catalyst, *Int. J. Hydrogen Energy*, 2024, **51**, 489–503, DOI: [10.1016/j.ijhydene.2023.07.054](https://doi.org/10.1016/j.ijhydene.2023.07.054).





- 89 A. A. Ceyhan, S. Edebalı and E. Fangaj, A study on hydrogen generation from  $\text{NaBH}_4$  solution using Co-loaded resin catalysts, *Int. J. Hydrogen Energy*, 2020, **45**, 34761–34772, DOI: [10.1016/j.ijhydene.2020.07.259](#).
- 90 Ş. Karakaya, E. Pehlivan and A. A. Ceyhan, Preparation of an efficient and reusable cobalt doped vermiculite ore catalyst for hydrogen production from sodium borohydride, *Int. J. Hydrogen Energy*, 2024, **73**, 282–293, DOI: [10.1016/j.ijhydene.2024.06.035](#).
- 91 L. Zhihua, Q. Li, F. Li, S. Zhao and X. Xia, Hydrogen generation from hydrolysis of  $\text{NaBH}_4$  based on high stable  $\text{NiB}/\text{NiFe}_2\text{O}_4$  catalyst, *Int. J. Hydrogen Energy*, 2017, **42**, 3971–3980, DOI: [10.1016/j.ijhydene.2016.10.115](#).
- 92 M. Yang, Y. Wu, Y. Liu, Z. Li, M. Cheng and C. Wu, *et al.*, Hydrogen production from hydrolysis of  $\text{NaBH}_4\text{-NH}_3\text{BH}_3$  composite catalyzed by porous spherical  $\text{Co}_3\text{O}_4$ , *Dig. J. Nanomater. Biostruct.*, 2023, **18**, 495–510, DOI: [10.15251/djnb.2023.182.495](#).
- 93 Y. Li, X. Hou, J. Wang, X. Feng, L. Cheng and H. Zhang, *et al.*, Co-Mo nanoparticles loaded on three-dimensional graphene oxide as efficient catalysts for hydrogen generation from catalytic hydrolysis of sodium borohydride, *Int. J. Hydrogen Energy*, 2019, **55**, 29075–29082, DOI: [10.1016/j.ijhydene.2019.02.124](#).
- 94 S. Zhou, Y. Yang, W. Zhang, X. Rao, P. Yan and T. Isimjan, *et al.*, Structure-regulated Ru particles decorated P-vacancy-rich CoP as a highly active and durable catalyst for  $\text{NaBH}_4$  hydrolysis, *J. Colloid Interface Sci.*, 2021, **591**, 221–228, DOI: [10.1016/j.jcis.2021.02.009](#).
- 95 Y. Zou, M. Nie, Y. Huang, J. Wang and H. Liu, Kinetics of  $\text{NaBH}_4$  hydrolysis on carbon-supported ruthenium catalysts, *Int. J. Hydrogen Energy*, 2011, **36**, 12343–12351, DOI: [10.1016/j.jcis.2021.02.009](#).
- 96 Y. Chen and H. Jin, Fabrication of amorphous Co–Cr–B and catalytic sodium borohydride hydrolysis for hydrogen generation, *J. Mater. Res.*, 2020, **35**, 281–288, DOI: [10.1557/jmr.2019.411](#).
- 97 Y. Wei, Y. Wang, L. Wei, X. Zhao, X. Zhou and H. Liu, Highly efficient and reactivated electrocatalyst of ruthenium electrodeposited on nickel foam for hydrogen evolution from  $\text{NaBH}_4$  alkaline solution, *Int. J. Hydrogen Energy*, 2018, **43**, 592–600, DOI: [10.1016/j.ijhydene.2017.11.010](#).
- 98 D.-R. Kim, K.-W. Cho, Y.-I. Choi and C.-J. Park, Fabrication of porous Co–Ni–P catalysts by electrodeposition and their catalytic characteristics for the generation of hydrogen from an alkaline  $\text{NaBH}_4$  solution, *Int. J. Hydrogen Energy*, 2009, **34**, 2622–2630, DOI: [10.1016/j.ijhydene.2008.12.097](#).
- 99 J. Zhang, F. Lin, L. Yang, Z. He, X. Huang and D. Zhang, *et al.*, Ultrasmall Ru nanoparticles supported on chitin nanofibers for hydrogen production from  $\text{NaBH}_4$  hydrolysis, *Chin. Chem. Lett.*, 2020, **31**, 2019–2022, DOI: [10.1016/j.cclet.2019.11.042](#).
- 100 A. Baye, M. Abebe, R. Appiah-Ntiamoah and H. Kim, Engineered iron-carbon-cobalt ( $\text{Fe}_3\text{O}_4@\text{C-Co}$ ) core-shell composite with synergistic catalytic properties towards hydrogen generation via  $\text{NaBH}_4$  hydrolysis, *J. Colloid Interface Sci.*, 2019, **543**, 273–284, DOI: [10.1016/j.jcis.2019.02.065](#).
- 101 H. Zhang, Q. Sun, L. Bian, Q. Peng, S. Han and B. Liu, *et al.*, Alloy-exciting effect of palladium-rhodium on MXene for enhanced hydrogen generation, *Int. J. Hydrogen Energy*, 2024, **49**, 1226–1235, DOI: [10.1016/j.ijhydene.2023.09.149](#).
- 102 E. Fangaj and A. A. Ceyhan, Apricot Kernel shell waste treated with phosphoric acid used as a green, metal-free catalyst for hydrogen generation from hydrolysis of sodium borohydride, *Int. J. Hydrogen Energy*, 2020, **45**, 17104–17117, DOI: [10.1016/j.ijhydene.2020.04.133](#).
- 103 E. Çalışkan and S. Göktürk, Adsorption characteristics of sulfamethoxazole and metronidazole on activated carbon, *Sep. Sci. Technol.*, 2010, **45**, 244–255, DOI: [10.1080/01496390903409419](#).
- 104 T. T. Van and J. P. Chang, Surface reaction kinetics of metal  $\beta$ -diketonate precursors with O radicals in radical-enhanced atomic layer deposition of metal oxides, *Appl. Surf. Sci.*, 2005, **246**, 250–261, DOI: [10.1016/j.apsusc.2004.11.025](#).
- 105 P. Behr, A. Terziyski and R. Zellner, Acetone Adsorption on Ice Surfaces in the Temperature Range  $T = 190\text{--}220\text{ K}$ : Evidence for Aging Effects Due to Crystallographic Changes of the Adsorption Sites, *J. Phys. Chem. A*, 2006, **110**, 8098–8107, DOI: [10.1021/jp0563742](#).
- 106 M. A. Gosálvez and J. Alberdi-Rodríguez, *A microscopic perspective on heterogeneous catalysis*, *arXiv*, 2018, preprint, arXiv:1812.11398, DOI: [10.48550/arXiv.1812.11398](#).
- 107 S. Kozuch and J. M. L. Martin, “Turning over” definitions in catalytic cycles, *ACS Catal.*, 2012, **2**, 2787–2794, DOI: [10.1021/cs3005264](#).
- 108 S. Anantharaj, P. E. Karthik and S. Noda, The significance of properly reporting turnover frequency in electrocatalysis research, *Angew. Chem., Int. Ed.*, 2021, **60**, 23051–23067, DOI: [10.1002/anie.202110352](#).
- 109 L. Shi, Z. Chen, Z. Jian, F. Guo and C. Gao, Carbon nanotubes-promoted Co–B catalysts for rapid hydrogen generation via  $\text{NaBH}_4$  hydrolysis, *Int. J. Hydrogen Energy*, 2019, **44**, 19868–19877, DOI: [10.1016/j.ijhydene.2019.05.206](#).
- 110 N. Patel, R. Fernandes and A. Miotello, Hydrogen generation by hydrolysis of  $\text{NaBH}_4$  with efficient Co–P–B catalyst: a kinetic study, *J. Power Sources*, 2009, **188**, 411–420, DOI: [10.1016/j.jpowsour.2008.11.121](#).
- 111 J. Zhao, H. Ma and J. Chen, Improved hydrogen generation from alkaline  $\text{NaBH}_4$  solution using carbon-supported Co–B as catalysts, *Int. J. Hydrogen Energy*, 2007, **32**, 4711–4716, DOI: [10.1016/j.ijhydene.2007.07.004](#).
- 112 M. A. Ababaii, N. Gilani and J. V. Pasikhani, Hydrogen evolution from  $\text{NaBH}_4$  solution using Cr-doped Ni–B metallic catalyst deposited on rice husk via electroless plating, *Int. J. Hydrogen Energy*, 2024, **51**, 648–662, DOI: [10.1016/j.ijhydene.2023.08.285](#).
- 113 H. Li, B. Li, Y. Zou, C. Xiang, H. Zhang and F. Xu, *et al.*, Modulating valence band to enhance the catalytic activity of Co–Cr–B/NG for hydrolysis of sodium borohydride, *J. Alloys Compd.*, 2022, **924**, 166556, DOI: [10.1016/j.jallcom.2022.166556](#).



- 114 S. Li, S. Qiu, Y. S. Chua, Y. Xia, Y. Zou and F. Xu, *et al.*, Co-B supported on waxberry-like hierarchical porous carbon microspheres: An efficient catalyst for hydrogen generation via sodium borohydride hydrolysis, *Mater. Chem. Phys.*, 2024, **319**, 129399, DOI: [10.1016/j.matchemphys.2024.129399](https://doi.org/10.1016/j.matchemphys.2024.129399).
- 115 H. Lakhali, S. Kocaman, G. Ahmetli and A. A. Ceyhan, Enhanced hydrogen generation in borohydride hydrolysis using an efficient and reusable IA-CNT supported Co-Mo-B catalyst, *Diam. Relat. Mater.*, 2025, 112364, DOI: [10.1016/j.diamond.2025.112364](https://doi.org/10.1016/j.diamond.2025.112364).
- 116 H. Cong, J. Ren, D. Zhang, F. Xu, X. Wang and Y. Wang, *et al.*, Catalytic hydrolysis of sodium borohydride for hydrogen generation using g-C<sub>3</sub>N<sub>4</sub>/Co-W-B/Ni foam composite catalyst, *J. Mater. Sci.*, 2023, **58**, 787–801, DOI: [10.1007/s10853-022-08073-z](https://doi.org/10.1007/s10853-022-08073-z).
- 117 C.-C. Chou, C.-H. Hsieh and B.-H. Chen, Hydrogen generation from catalytic hydrolysis of sodium borohydride using bimetallic Ni-Co nanoparticles on reduced graphene oxide as catalysts, *Energy*, 2015, **90**, 1973–1982, DOI: [10.1016/j.energy.2015.07.023](https://doi.org/10.1016/j.energy.2015.07.023).
- 118 M. Zahmakiran and S. Ozkar, Zeolite-confined ruthenium (0) nanoclusters catalyst: record catalytic activity, reusability, and lifetime in hydrogen generation from the hydrolysis of sodium borohydride, *Langmuir*, 2009, **25**, 2667–2678, DOI: [10.1021/la803391c](https://doi.org/10.1021/la803391c).
- 119 H. Li, J. Liao, X. Zhang, W. Liao, L. Wen and J. Yang, *et al.*, Controlled synthesis of nanostructured Co film catalysts with high performance for hydrogen generation from sodium borohydride solution, *J. Power Sources*, 2013, **239**, 277–283, DOI: [10.1016/j.jpowsour.2013.03.167](https://doi.org/10.1016/j.jpowsour.2013.03.167).
- 120 H. Lakhali, A. A. Ceyhan and Ö. Şahin, Novel Fe<sub>3</sub>O<sub>4</sub>@SiO<sub>2</sub>/Co-Mo-B core-shell magnetic nanocatalyst: A reusable system for high-performance hydrogen evolution in borohydride hydrolysis, *Inorg. Chem. Commun.*, 2025, 114406, DOI: [10.1016/j.inoche.2025.114406](https://doi.org/10.1016/j.inoche.2025.114406).

